AGU PUBLICATIONS

JGR

Journal of Geophysical Research: Solid Earth

RESEARCH ARTICLE
10.1002/2016JB013549

Key Points:
- We present updated geological slip rates for the Sumatran Fault and a new continuous GPS velocity field of Sumatra, Indonesia
- In contrast with previous studies that proposed trench-parallel stretching of the Sumatran fore arc, we instead infer a rigid fore-arc block
- Deformation within the Wharton Basin oceanic lithosphere plays a critical role in slip partitioning of oblique plate convergence

Correspondence to:
K. E. Bradley,
kbradley@ntu.edu.sg

Citation:
Bradley, K. E., L. Feng, E. M. Hill, D. H. Natawidjaja, and K. Sieh (2017), Implications of the diffuse deformation of the Indian Ocean lithosphere for slip partitioning of oblique plate convergence in Sumatra, *J. Geophys. Res. Solid Earth*, *122*, 572–591, doi:10.1002/2016JB013549.

Received 21 SEP 2016
Accepted 2 DEC 2016
Accepted article online 6 DEC 2016
Published online 4 JAN 2017

Implications of the diffuse deformation of the Indian Ocean lithosphere for slip partitioning of oblique plate convergence in Sumatra

K. E. Bradley[1], L. Feng[1], E. M. Hill[1,2], D. H. Natawidjaja[3], and K. Sieh[1,2]

[1]Earth Observatory of Singapore, Nanyang Technological University, Singapore, [2]Asian School of the Environment, Nanyang Technological University, Singapore, [3]Research Center for Geotechnology, Indonesian Institute of Geosciences (LIPI), Bandung, Indonesia

Abstract Oblique plate convergence between Indian Ocean lithosphere and continental crust of the Sunda plate is distributed between subduction on the Sunda megathrust and upper plate strike-slip faulting on the Sumatran Fault Zone, in a classic example of slip partitioning. Over the last decade, a destructive series of great earthquakes has brought renewed attention to the mechanical properties of these faults and the intervening fore-arc crustal block. While observations of fore-arc deformation over the earthquake cycle indicate that the fore-arc crust is fundamentally elastic, the spatial pattern of slip vector azimuths for earthquakes sourced by rupture of the Sunda megathrust is strongly inconsistent with relative motion of two rigid plates. Permanent and distributed deformation therefore occurs in either the downgoing lithospheric slab or the overriding fore-arc crust. Previous studies have inferred from geodetic velocities and geological slip rates of the Sumatran Fault that the fore-arc crust is undergoing rapid trench-parallel stretching. Using new geological slip rates for the Sumatran Fault and an updated decadal GPS velocity field of Sumatra and the fore-arc islands, we instead show that permanent deformation within the fore-arc sliver is minor and that the Sumatran Fault is a plate boundary strike-slip fault. The kinematic data are best explained by diffuse deformation within the oceanic lithosphere of the Wharton Basin, which accommodates convergence between the Indian and Australian plates and has recently produced several large earthquakes well offshore of Sumatra. The slip partitioning system in Sumatra is fundamentally linked with the mechanical properties of the subducting oceanic lithosphere.

1. Introduction

The Indonesian island of Sumatra (Figure 1) is widely recognized as a type of locality for slip partitioning of oblique plate convergence [*Fitch*, 1972; *Jarrard*, 1986]. Relative plate motion is accommodated by a combination of low-obliquity subduction along the Sunda megathrust and strike-slip faulting within the upper plate along the Sumatran Fault zone. These great fault systems are separated by an elongate and narrow crustal sliver, which in Sumatra consists of the entire region between the active volcanic arc and the subduction trench. However, while the Sumatran margin at first appears to be a relatively simple arrangement of three plates, slip vector azimuths for earthquake ruptures of the Sunda megathrust (Figure 2) cannot be described by a single angular velocity vector [*McCaffrey*, 1991] and are therefore inconsistent with relative motion of a rigid fore arc and a rigid subducting slab [*McKenzie and Parker*, 1967]. Previous studies have resolved this inconsistency by inferring rapid, permanent deformation of the fore-arc crust [*McCaffrey*, 1991, 1992]. In such models (Figure 2), trench-parallel stretching of the fore-arc sliver above a rigid oceanic plate explains the systematic change in megathrust slip vector azimuths and requires a strong northward increase of the slip rate of the Sumatran Fault [*McCaffrey et al.*, 2000].

However, a variety of observations also require long-lived and continuing deformation of the oceanic lithosphere offshore of Sumatra (Figure 1). These include predominantly strike-slip earthquakes within the oceanic lithosphere offshore of Sumatra and within the subducting slab [*Fauzi et al.*, 1996; *Abercrombie et al.*, 2003; *Ishii et al.*, 2013; *Hill et al.*, 2015], the complex seafloor geology of the Wharton Basin [*Gordon et al.*, 1990; *Royer and Gordon*, 1997; *Deplus et al.*, 1998; *Andrade and Rajendran*, 2014], and relative motion of Australia and India observed by space geodesy [*Delescluse and Chamot-Rooke*, 2007; *DeMets et al.*, 2010]. A component of trench-parallel lithospheric shortening within the Wharton Basin, in combination with a rigid Sumatran fore arc, could also adequately explain the Sunda megathrust slip vector azimuths. In this case, we would expect the Sumatran Fault to exhibit a roughly uniform slip rate along its entire length.

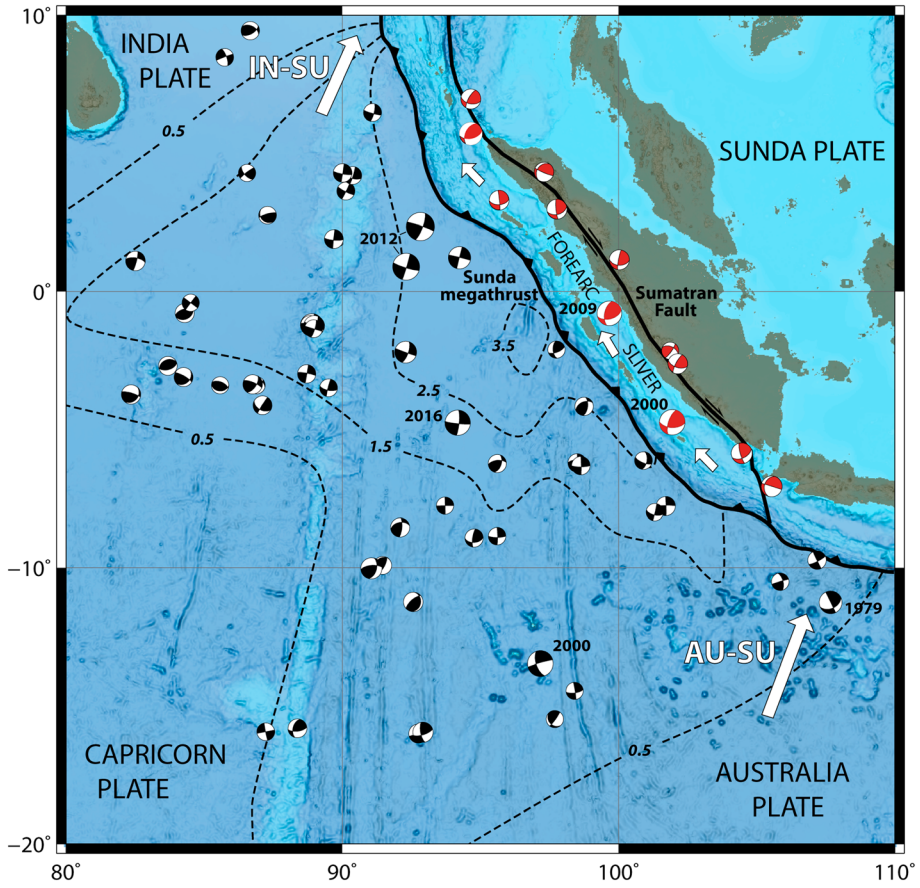

Figure 1. Diffuse seismicity within the oceanic lithosphere of the Wharton Basin and the subducted slab beneath Sumatra. Seismicity of the Sunda megathrust and Sumatran Fault are not shown. Intraplate deformation within the subducted oceanic slab beneath the Sumatran fore arc is evidenced by deep strike-slip earthquakes (red). The approximate spatial distribution of offshore deformation is indicated by dashed lines representing contours of the second invariant of the strain rate tensor ($\times 10^{-16}$ s^{-1}) from a regional model of diffuse deformation [*Gordon and Houseman*, 2015]. Australia-Sunda (AU-SU) and India-Sunda (IN-SU) plate motions are from MORVEL [*DeMets et al*., 2010]; motion of the fore arc relative to Sunda is schematic.

The slip rate of the Sumatran Fault Zone is therefore a primary, and readily measurable, aspect of the slip partitioning system. Published and unpublished (but commonly cited) Late Quaternary geological slip rates for the Sumatran Fault (Figure 3) show a systematic increase from south to north [*McCaffrey et al*., 2000; *Bellier and Sébrier*, 1995; *Detourbet et al*., 1993; *Sieh et al*., 1991], and geodetic studies of the decadal velocity field appear to agree with this assessment [*Genrich et al*., 2000]. This agreement between geological and geodetic results has resulted in widespread acceptance of the fore-arc stretching model.

In this study, we present updated geological slip rates for the Sumatran Fault and new GPS velocities from the Sumatra GPS Array (SuGAr). We evaluate the character of slip partitioning using a kinematic block model and a local force balance analysis that are both designed to incorporate the internal deformation of the Wharton Basin. Based on these models, we propose that all of the available kinematic data are best explained by a rigid fore-arc sliver overlying a heterogeneously coupled Sunda megathrust. The sliver plate moves relative to Sunda at a rate that is consistent with reliable geological slip rate estimates for the Sumatran Fault.

2. Existing Sumatran Fault Slip Rates

Due to dense vegetative cover and inaccessibility, few geological slip rate estimates have been published for the Sumatran Fault. While the available results exert an outsized influence on our understanding of the tectonics of the Sumatran margin, they are commonly cited without consideration of their relative reliability [*Ito*

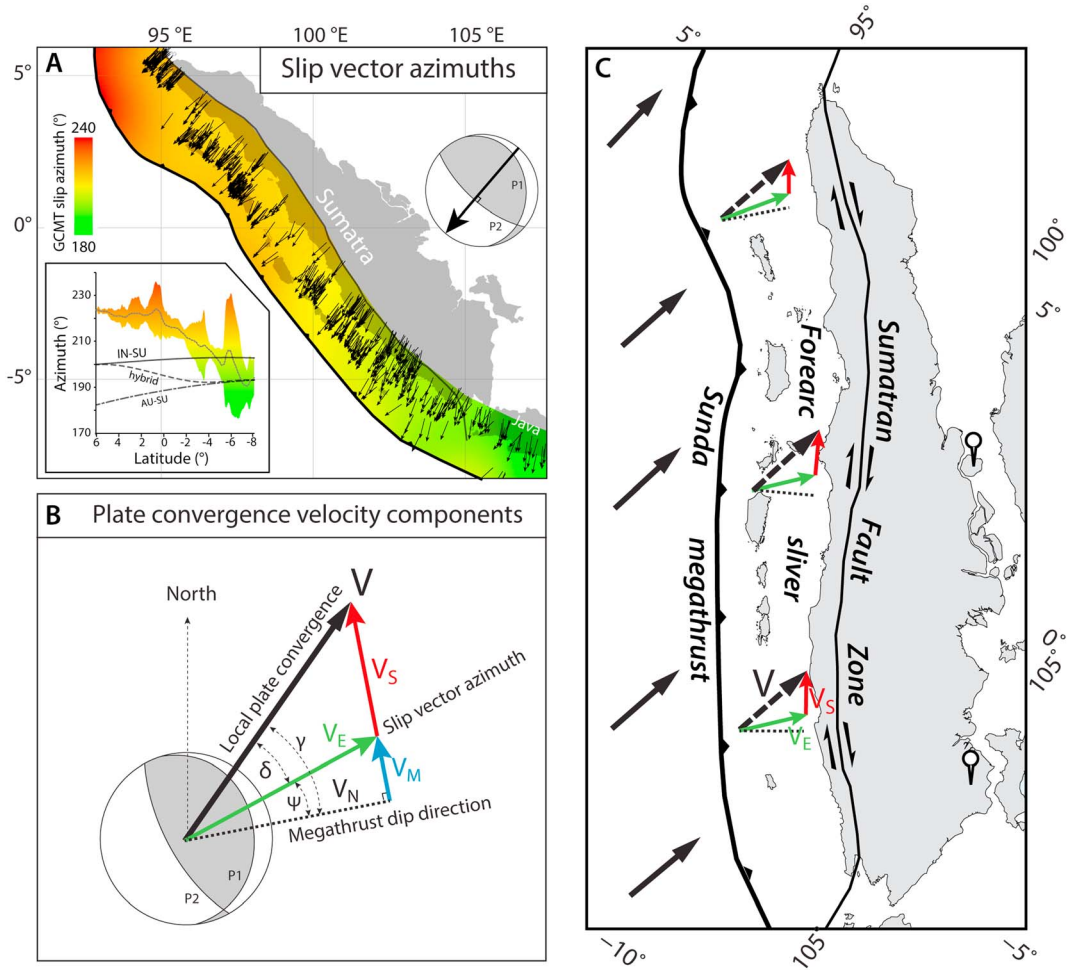

Figure 2. (a) Slip vector azimuths of earthquakes that resulted from rupture of the Sunda megathrust or (more rarely) reverse faults within the fore-arc crust and accretionary wedge, selected from the Global Centroid Moment Tensor catalog [*Ekström et al*., 2012]. There is a smooth variation from nearly north-south underthrusting beneath West Java to northeast-southwest underthrusting beneath North Sumatra, which cannot be explained by a single angular velocity vector describing relative motion of the fore-arc sliver and the subducting slab. IN-SU: MORVEL India-Sunda plate convergence [*DeMets et al*., 2010]. AU-SU: MORVEL Australia-Sunda plate convergence. Hybrid model: a nonplate model that smoothly transitions from AU-SU to IN-SU convergence between 4°N and 4°S. (b) Components of plate convergence velocity (relative to Sunda) in a simply partitioned system and their estimation from focal mechanisms [*McCaffrey*, 1992]. The strike-slip fault parallels the strike of the obliquely slipping megathrust. V_S: predicted slip rate of the strike-slip fault; V_M: strike-parallel component of convergence velocity accommodated by oblique slip on the megathrust; V_E: velocity of underthrusting beneath the fore arc. V_N: margin-normal convergence velocity. γ: convergence obliquity between the subducting slab and the stationary upper plate. δ: angle between the plate convergence direction and the direction of underthrusting beneath the fore arc. Ψ: obliquity of underthrusting of the oceanic slab beneath the fore arc. (c) Map view of a simplified slip partitioning system in Sumatra, in which oblique plate convergence is distributed onto two plate boundary faults. Representative velocity vectors are relative to a stationary Sunda block (pinned). Vector colors are the same as in Figure 2b.

et al., 2012; *Ishii et al*., 2013]. In order to clarify the assumptions and observations that underlie the available slip rates for the Sumatran Fault, we here offer a critical evaluation of all commonly cited slip rates from north to south (Figure 3), with focus on documenting the proposed offsets and age constraints for each slip rate estimate.

Bennett et al. [1981] documented the basic geological setting of the Sumatran Fault in Aceh province (northern Sumatra) and indicated several locations where long-term slip rates could theoretically be measured. However, this study did not include a proposed slip rate. The 38 ± 4 mm/yr slip rate for which this study is commonly cited [*Ito et al*., 2012] was inferred by *Genrich et al*. [2000] for the purpose of comparison

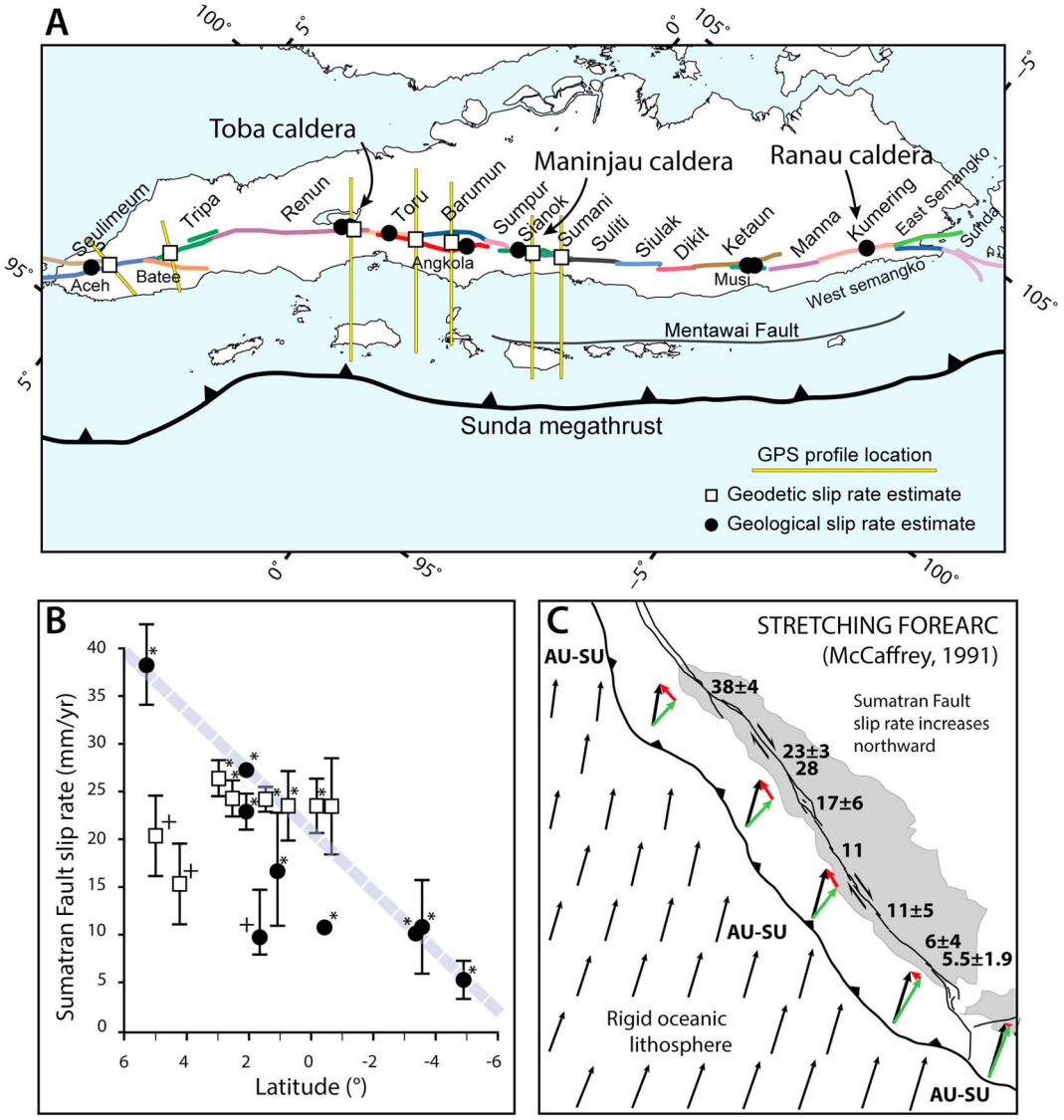

Figure 3. (a) Locations of published (and unpublished but commonly cited) geological and geodetic slip rate estimates for different segments in the Sumatran Fault. The primary fault segments are drawn in different colors based on *Sieh and Natawidjaja* [2000]. (b) The slip rate data appear to show a northward increase from 5 mm/yr in South Sumatra to >30 mm/yr in North Sumatra. We suggest that rates marked with an asterisk are unreliable; these are discussed in the main text. Rates marked with a cross were not available to earlier studies. The dashed line schematically indicates the northward increase in Sumatran Fault slip rates. (c) A northward increase in the slip rate of the Sumatran Fault [e.g., *McCaffrey*, 1991] explains the Sunda megathrust slip vector azimuth variation and requires stretching of the fore arc between the Sunda megathrust and the Sumatran Fault. Plate convergence velocities are derived from the MORVEL Australia-Sunda angular velocity. Velocity components of sites located on the fore-arc sliver (colored vectors are defined in Figure 2) are shown schematically.

with geodetic results but was not proposed to be a reliable slip rate and should therefore not be cited as an actual estimate. The AGNeSS GPS array measured right-lateral elastic strain accumulation rates of 16 ± 6 mm/yr across the Aceh segment and 20 ± 6 mm/yr across the parallel Aceh and Seulimeum segments between 2005 and 2010 [*Ito et al.*, 2012].

Slip rates for several segments of the Sumatran Fault are commonly cited from meeting abstracts [*Sieh et al.*, 1991, 1994]. Based on measured deflections of the river systems discussed in section 3, these authors proposed a slip rate of 10–11 mm/yr for the Sianok segment near Bukittinggi (0.2°S) [see also *Yeats et al.*, 1997] and 27–28 mm/yr for the Renun segment at Toba (2.3°N). The latter value is similar to a slip rate of 23 ± 3 mm/yr at 2.3°N that is also based on deflection of river channels incised into the Young Toba Tuff [*Detourbet et al.*, 1993]. Each of these studies relied on small-scale topographic maps or SPOT satellite imagery

that were of insufficient resolution to distinguish between actual channel offsets and channel deflections within 500 m of the fault trace, and no detailed offset maps have been presented to date. In the following sections of this paper, we will revise the slip rate estimates for Toba and Maninjau using updated mapped offsets and more recent chronometric constraints.

A geological slip rate of 7–14 mm/yr is available for the Toru segment (1.6°N) of the Sumatran Fault where it traverses the Sibuabuali volcano [*Hickman et al*., 2004]. This slip rate is based on a mapped lateral offset of a dacite dome dated by incremental heating $^{40}Ar/^{39}Ar$ to 270 ± 3 ka, with the primary source of slip rate uncertainty being the mapped lateral offset. At this latitude, the northern section of the Angkola segment also traverses the western side of 0.7–0.3 Ma Sibualbuali volcanic edifice, parallel to the Toru segment. The total slip rate of the Sumatran Fault System at this latitude could be greater than the reliably constrained minimum slip rate of 7–14 mm/yr.

The Musi segment at 3.5°S exhibits systematic right-lateral deflections of volcanic lava flows that could be used to constrain the Late Pleistocene or Holocene slip rate; however, no maps of geomorphic offsets or age control have been presented, and the available 10 mm/yr slip rate estimate [*Sieh et al*., 1994] cannot be cited as a definitive estimate.

The slip rate of the Sumatran Fault has also been constrained in areas where multiple river channels exhibit differing apparent lateral offsets, based on an assumed linear relationship between channel length and channel age [*Bellier and Sébrier*, 1994]. In this study, the relationship between channel length and age was calibrated using observations from offset channel lengths at Toba, assuming the 23 ± 2 mm/yr slip rate of *Detourbet et al*. [1993]. This approach yields estimated slip rates of 17 ± 6 mm/yr at 1°N (the Angkola segment) and 11 ± 5 mm/yr at 3–4°S (the Musi segment). However, the assumption that channels incised into young volcanic units grow in length at a constant rate is clearly violated along the Sianok and Renun segments, where isochronous channels of many lengths occur. Channel age is tied to the eruption age of the substrate, channel lengths are mostly controlled by the spatial arrangement of preeruption drainage divides, and rates of incision and headward erosion are known to decline rapidly in posteruption landscapes as landscapes quickly readjust [*Manville et al*., 2009]. We suggest that these slip rates be considered speculative until direct age control for the offset channels is achieved.

A 6 ± 4 mm/yr slip rate for the Kumering segment in southern Sumatra is based on an apparent separation of an interpreted tectonic lineament mapped on SPOT imagery [*Bellier et al*., 1991]. This rate was later revised to 5.5 ± 1.9 mm/yr based on a $^{40}K-^{40}Ar$ age of 0.55 ± 0.15 Ma (2 SD, N = 4) for a single sample of tuff attributed to the youngest paroxysmal eruption of the Ranau Caldera, and proposed posteruption right-lateral geomorphic offsets of ~2.5 km [*Bellier et al*., 1999]. The Ranau Tuff has a fresh geomorphic appearance and is not buried by later eruptive units, and the lateral geomorphic offsets proposed by *Bellier et al*. [1999] are not clearly supported by modern satellite imagery, we suggest that this slip rate estimate is also unreliable.

With the exception of the minimum slip rate estimate of *Hickman et al*. [2004], the published or commonly cited geological slip rates for the Sumatran Fault are not based on accurate dating of adequately mapped geological or geomorphic offsets (Figures 3b and 3c). No firm conclusions about the average fault slip rate or the along-strike-slip rate variation of the Sumatran Fault can be drawn from these data. We have therefore revisited several key localities where slip rates can be readily estimated from systematic offsets of channels incised into young caldera outflow sheets.

3. Revised Sumatran Fault Slip Rates From Offset Caldera Tuffs

The time-averaged slip rate of the Sumatran Fault is best recorded by lateral offsets of multiple isochronous river channels incised into young caldera tuffs, in areas where the Sumatran Fault has only one main active trace. We mapped deflected river channels and ridge crests along the Sianok and Renun segments of the Sumatran Fault using ASTER GDEM (30 m), TerraSAR World30 (30 m), and SRTM (30 m) topographic data combined with high-resolution satellite imagery taken at low off-nadir angles (QuickBird and WorldView-2 at 0.5 m resolution) and field observations. Where it traverses young nonwelded tuffs, the Sumatran Fault is typically expressed as a 50–500 m wide zone marked by isolated raised hills or a fault-parallel river valley. Due to ongoing channel widening, primarily by landslides, and fault-related deformation and erosion within

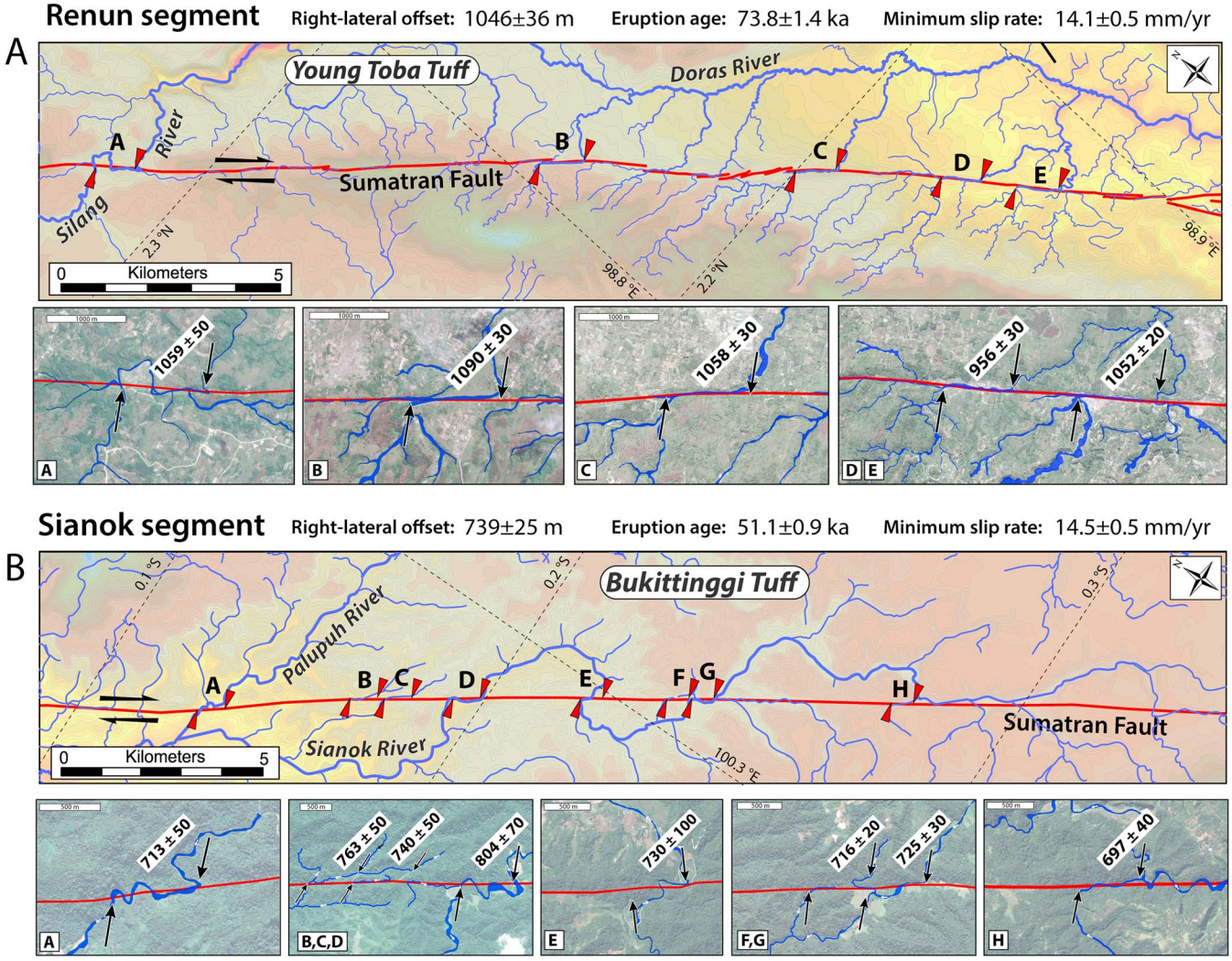

Figure 4. Geological slip rates for the Renun and Sianok segments (refer to Figure 3 for locations). At each locality, systematic lateral offsets of isochronous channels incised into thick caldera tuffs over 20 km of along-fault distance yield an estimate of the average slip rate since eruption. Channel offsets are labeled in meters, with uncertainties estimated from the width of the laterally offset feature. (a) The minimum slip rate of the Renun segment (14.1 ± 0.5 mm/yr) is significantly lower than previous estimates of 21–26 mm/yr. (b) The minimum slip rate of the Sianok segment (14.5 ± 0.5 mm/yr) is higher than previous estimates of 11 mm/yr. Constraints on the eruption ages are discussed in the text.

100 m of the fault trace, we cannot typically identify piercing lines. Instead, at each locality we project sets of ridge crests and contour lines defining the steep margins of the river channel that are well defined within 200 m of the fault and bring those projected lines into approximate alignment. The precision of our estimated best fit offset varies between localities, with the most confident matches having an approximate uncertainty of 20–30 m and the least confident matches 50–100 m, mostly depending on the width of the offset channel.

3.1. Slip Rate of the Renun Segment at Toba (2.3°N)

West of Toba Caldera, the Renun segment of the Sumatran Fault traverses the Young Toba Tuff (Figure 4a). The eruption age of this voluminous tephra is well constrained. Early studies using $^{40}K/^{40}Ar$ and $^{40}Ar/^{39}Ar$ chronometry yielded eruption ages between 73 ± 8 ka and 74.9 ± 12 ka [*Ninkovich et al.*, 1978; *Chesner et al.*, 1991]. More recent high-precision $^{40}Ar/^{39}Ar$ single-grain laser fusion ages range between 72.7 ± 8.2 ka and 74.2 ± 1.8 ka [*Mark et al.*, 2014; *Storey et al.*, 2012]. We adopt an eruption age of 73.88 ± 0.64 ka that is based on single-grain fusion dating of sanidine separated from a distal Young Toba

Tuff ash bed in Malaysia [*Storey et al*., 2012] as the age of eruption of the Young Toba Tuff and widespread resetting of the geomorphic landscape in the vicinity of the caldera.

Prior to eruption of the Young Toba Tuff, the landscape of the southern Renun segment was characterized by a mountainous upland separated from a broad valley by the linear trace of the Sumatran Fault. The Young Toba Tuff blanketed the region with over 100 m of tephra, filling the fault-bounded valley and capping the surrounding mountain ranges. River channels between 10 and 100 m deep were subsequently incised into the uppermost, nonwelded part of the tuff, across, and in most cases at high angle to the trace of the Sumatran Fault. We identify 14 river channels that originate in the western highland area and exhibit right-stepping lateral deflections where they cross the trace of the Sumatran Fault (Figure 4a). Of these, we select five channels as being the most representative of the total displacement due to their larger drainage areas and relatively deep incision into the Young Toba Tuff. At one site, the Silang River is offset dextrally before flowing into the Toba caldera lake. At four other sites, tributary channels of the southeast-flowing Doras River cross the Sumatran Fault at high angle and are dextrally offset. Notably, restoration of any offset greater than 1 km yields untenable reconstructions for the most deeply incised channels. The average of the five channel offsets is 1043 ± 36 m, yielding a posteruption right-lateral slip rate of 14.1 ± 0.5 mm/yr that is significantly lower than previous estimates [*Sieh et al*., 1991; 1994; *Detourbet et al*., 1993].

3.2. Slip Rate of the Sianok Segment at Maninjau (0.2°S)

The Sianok segment of the Sumatran Fault traverses the Bukittinggi Tuff (Figure 4b), which was erupted during formation of the Maninjau caldera and subsequently incised by the Sianok and Palupuh rivers [*Sieh and Natawidjaja*, 2000]. The Bukittinggi Tuff has been dated by a combination of ^{14}C and glass fission track techniques [*Alloway et al*., 2004; *Ascough et al*., 2009]. While the inferred age of 51–52 ka lies outside of the typical range of applicability of either technique, it is unlikely that the tuff is much younger than the stated estimate and that the resulting Sumatran Fault slip rate is significantly underestimated. We adopt an eruption age of 51.1 ± 0.9 ka, calculated as a nonweighted mean of the ^{14}C and GFT ages [*Alloway et al*., 2004; *Ascough et al*., 2009].

The Palupuh River crosses the fault trace and joins the Sianok River near the western contact between the Bukittinggi Tuff and older rock units. East of the Maninjau caldera, the sinuous Sianok River crosses the Sumatran Fault at high angle (55–80°) at five separate locations. The lack of an apparent upstream decrease in the magnitude of channel deflections of the Sianok River indicates that incision and headward erosion were too fast to capture significant slip accumulation on the fault, counter to a steady channel growth model [*Bellier and Sébrier*, 1994]. The slip rate calculated from eight geomorphic offsets is 14.5 ± 0.5 mm/yr, somewhat faster than previous estimates.

3.3. Timing of Posteruption Incision of Tuffs in Sumatra

We calculate the long-term fault slip rates at Maninjau and Toba under the assumption that significant incision and establishment of river channel geometries across the fault occurred very soon after eruption. Notably, significantly delayed incision would result in faster long-term slip rates. The combination of steep initial surface slope, easily eroded nonwelded tuffs lacking the modern thick soil and vegetative cover, and high discharge rate due to the tropical environment, suggest that incision rates would have been very high. Observations of historical and geologically recent ($<$10,000 ka) eruptions that emplaced thick, non-welded tuff units show that landscape adjustment from the smooth and hydrologically deranged surface of the ejecta blanket into an incised, dendritic, or parallel fluvial network occurs within years to decades of eruption [*Manville et al*., 2009]. It is therefore likely that the first few meters of incision that established the basic geometry of the subsequently offset channels at Maninjau and Toba occurred very soon after eruption.

4. Updated GPS Velocity Field for Sumatra

GPS velocities of sites located on mainland Sumatra and the fore-arc islands (Figure 5) depend strongly on how slip is partitioned between the Sunda megathrust and strike-slip faults in the upper plate and have long served as a primary constraint on kinematic models of this region [*McCaffrey et al*., 2000; *Genrich et al*., 2000; *Prawirodirdjo et al*., 2010]. Here we present updated long-term GPS velocities from the continuous Sumatran

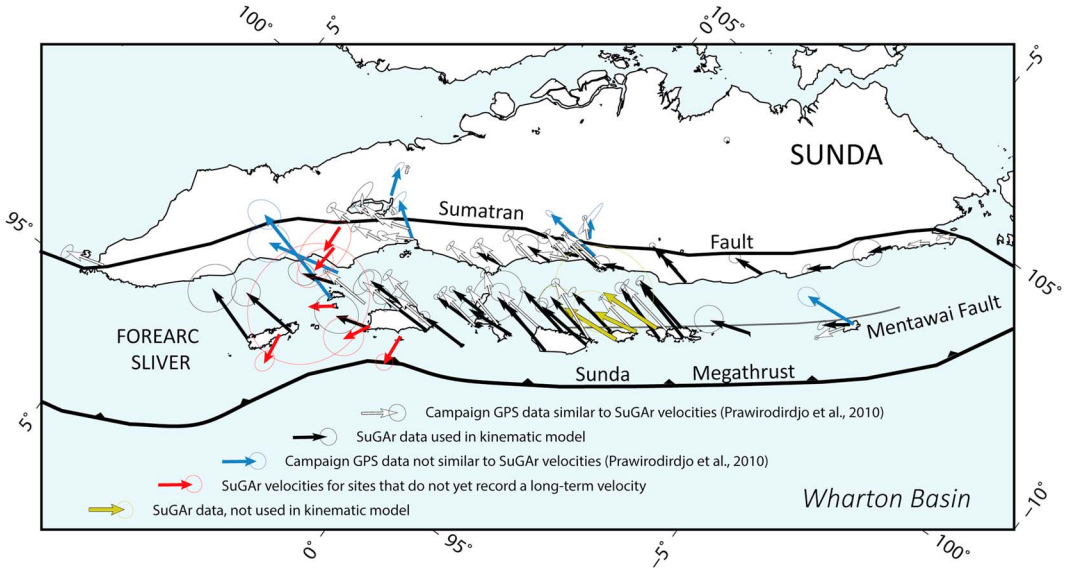

Figure 5. Sumatran GPS site velocity data used in this study. Campaign mode GPS sites are from *Prawirodirdjo et al.* [2010] and mainly reflect interseismic strain accumulated prior to the cascade of great earthquakes that began with the 25 December 2004 event. We exclude seven site velocities due to unexplained inconsistencies with multiple nearby sites, either due to unresolved local effects or different epochs of observation. Continuous GPS site velocities are from the SuGAr network as reported in this study (Table 1). We exclude six recently installed sites due to large trenchward velocity components that cannot reflect long-term strain accumulation from frictional locking of the megathrust. We also exclude three sites in the Mentawai island region that show anomalously large trench-parallel velocities that are at odds with nearby site velocities. Plotted uncertainty ellipses for the SuGAr cGPS velocities reflect the weighting applied in our block model and are significantly larger than the analytical uncertainties.

GPS Array (SuGAr) that extend the spatial and temporal coverage of strain accumulation in the fore arc. Stations in this array were installed as early as 1998 and have operated for as long as 13 years, although most stations were installed following the great earthquake of 2004. The details of GPS processing and analysis of SuGAr data [*Feng et al.*, 2015] are only briefly summarized here. Notably, in order to recover the most reliable long-term site velocities, many nontectonic physical effects are modeled in the GPS processing [*Feng et al.*, 2015]. The remaining signals included large seasonal and earthquake-related effects that are further removed in the postprocessing. We first process the RINEX data using GIPSY-OASIS version 6.2. The resulting daily position time series are represented in the International Terrestrial Reference Frame 2008 (ITRF2008) and are transferred to the Sunda plate reference frame using the Sunda-ITRF2008 angular rotation [*Altamimi et al.*, 2012]. Most SuGAr time series are affected by coseismic and postseismic transient deformation resulting from a series of moderate to great earthquakes that began with the 2004 M_w 9.2 Sumatran-Andaman earthquake. We remove from the time series coseismic offsets from 30 earthquakes with $M_w \geq 5.9$ and postseismic decays from 10 earthquakes with $M_w \geq 6.7$ [*Feng et al.*, 2015], resulting in final estimates for long-term site velocities (Table 1). These velocities represent our best estimation of long-term deformation least affected by transients associated with earthquakes. Eight stations installed since late 2010 are strongly affected by earthquake signals. We report the current best estimate of the long-term velocity of these sites but consider them to be highly unreliable, as indicated by their large trenchward velocity component (Table 2). We exclude three site velocities located on the Mentawai fore-arc islands (2–3°S) from our subsequent kinematic modeling due to unresolved but significant discrepancies with nearby campaign or continuous site velocities. These sites would exert little influence on model results due to the high density of sites in this area. For most sites, the long-term velocities depend strongly on rates before the 2004, 2005, and 2007 great Sumatran earthquakes and are similar in magnitude and azimuth to interseismic campaign mode measurements that largely predate the 2004 event [*Prawirodirdjo et al.*, 2010].

5. Slip Partitioning Viewed as a Local Frictional Balance

Slip partitioning can be envisioned as resulting from a local frictional balance between the megathrust and the upper plate strike-slip fault, under a given plate convergence model with a rigid subducting plate

Table 1. SuGAr GPS Long-Term Site Velocities Relative to Sunda

Site	Longitude (°E)	Latitude (°N)	Height (m)	Installation (year/month/day)	ΔT (years)	Relative to Sunda (mm/yr)					
						N	1σ	*E*	1σ	*U*	1σ
ABGS	99.3875	0.2208	236.25	2004/9/4	9.32	17.9	0.2	−3.6	0.2	−0.3	0.5
BITI	97.8114	1.0786	7.07	2005/11/26	8.08	28.9	0.4	0.0	0.4	0.9	0.9
BSAT	100.2846	−3.0767	6.25	2002/9/21	11.25	42.4	0.1	10.9	0.1	−10.2	0.3
BSIM	96.3262	2.4092	21.26	2005/2/1	8.90	37.6	1.5	2.8	0.8	−2.7	2.2
BTET	98.6439	−1.2815	21.58	2005/11/16	8.11	38.5	0.1	9.4	0.1	−8.7	0.4
BTHL	97.7106	0.5692	67.85	2005/8/16	8.37	36.2	0.3	0.3	0.3	−5.5	0.6
BUKT	100.3181	−0.2019	850.22	2010/2/11	3.86	4.6	0.2	−4.4	0.2	4.0	0.6
JMBI	103.5203	−1.6156	62.83	2005/4/14	8.70	2.1	0.1	1.3	0.1	0.0	0.3
KTET[a]	99.8407	−2.3625	35.20	2008/1/26	5.90	28.6	0.8	−5.8	0.6	−10.2	1.5
KRUI	103.8547	−5.0902	60.39	2011/11/7	2.15	9.4	0.5	−12.1	0.5	−1.3	1.5
LAIS	102.0339	−3.5292	20.48	2006/3/4	7.82	19.9	0.2	−2.0	0.2	−1.8	0.6
LEWK	95.8041	2.9236	7.06	2005/2/4	8.88	36.7	0.8	11.9	0.9	1.6	1.6
LHWA	97.1345	1.3835	21.73	2005/2/14	2.55	21.3	0.8	−6.5	0.7	−23.0	2.3
LNNG	101.1565	−2.2853	40.10	2004/8/22	9.36	22.1	0.1	3.5	0.1	−1.8	0.3
MKMK	101.0914	−2.5427	0.54	2004/8/23	9.35	23.8	0.1	4.8	0.1	−1.7	0.4
MLKN	102.2765	−5.3526	17.12	2005/8/2	8.41	14.2	0.1	−11.2	0.2	−5.4	0.5
MNNA	102.8903	−4.4503	28.54	2006/2/28	7.84	11.9	0.1	−10.4	0.2	−1.9	0.4
MSAI	99.0895	−1.3264	29.18	2002/8/8	11.39	36.3	0.1	6.5	0.1	−4.8	0.4
NGNG	99.2683	−1.7997	46.28	2004/8/14	9.32	37.2	0.3	7.1	0.5	−9.8	1.1
NTUS	103.6800	1.3458	75.39	2001/6/18	12.53	0.9	0.1	0.1	0.1	0.6	0.2
PARY	100.3186	−0.7526	109.90	2010/1/16	3.95	10.1	0.1	−4.7	0.2	2.1	0.5
PBAI	98.5262	−0.0316	1.06	2002/8/15	3.61	25.0	0.1	0.3	0.1	3.8	0.4
PBJO	98.5157	−0.6365	35.91	2005/8/12	8.38	31.6	0.3	−2.8	0.3	−2.1	0.3
PBLI	97.4053	2.3085	−9.61	2005/8/19	8.36	20.2	0.5	−7.5	0.4	6.3	0.8
PKRT[a]	99.5428	−2.1514	31.82	2007/9/10	6.30	37.9	1.0	−3.4	0.6	−16.6	1.4
PPNJ	99.6037	−1.9940	34.88	2005/4/20	8.70	34.6	0.1	5.2	0.2	−4.9	0.5
PRKB	100.3996	−2.9666	21.84	2004/8/07	9.39	39.4	0.1	8.3	0.2	−7.7	0.5
PSKI	100.3534	−1.1247	48.30	2002/8/05	11.40	23.2	0.1	1.1	0.1	−1.5	0.3
PSMK	97.8609	−0.0893	9.48	2002/8/19	11.36	31.1	0.2	0.5	0.2	−4.3	0.5
PTLO	98.2800	−0.0546	15.90	2002/8/17	11.37	27.1	0.1	−0.2	0.1	−0.2	0.4
SAMP	98.7147	3.6216	1.89	1998/8/31	13.21	4.2	0.0	0.3	0.0	−11.9	0.1
SLBU	100.0097	−2.7664	2.79	2004/8/9	9.38	39.2	0.2	11.3	0.2	−10.4	0.6
SMGY	100.1026	−2.6145	6.94	2008/1/22	5.93	40.2	1.8	−1.9	1.5	−18.0	2.4
TIKU	99.9442	−0.3991	18.79	2006/3/8	4.82	17.2	0.4	−1.0	0.4	−2.1	1.0
TLLU[a]	99.1341	−1.8003	97.91	2009/1/1	4.99	37.5	0.2	2.8	0.2	−11.4	0.5
TNTI	98.7315	−0.9667	20.49	2011/1/1	1.51	33.7	0.8	6.2	1.0	0.9	2.6
TRTK	100.6242	−1.5208	125.39	2010/2/15	3.87	13.4	0.3	−6.3	0.3	−0.1	0.7

[a]Sites not included in kinematic model due to large uncertainties and significant differences from both campaign velocities and nearby SuGAr stations.

[*McCaffrey*, 1991, 1994]. In this case, any along-strike variation of the inferred slip rate of the strike-slip fault would require internal deformation of the fore-arc sliver. In order to adequately explore the possible plate convergence scenarios, we estimate the slip rate of the Sumatran Fault for three models: one assuming MORVEL AU-SU convergence, one assuming MORVEL IN-SU convergence, and one assuming a hybrid

Table 2. SuGAr GPS Velocities Relative to the Sunda Plate, Not Interpreted as Long-Term Due To Recent Installation and Significant Remaining Effects of Earthquakes

Site	Longitude (°E)	Latitude (°N)	Height (m)	Installation (year/month/day)	ΔT (years)	Relative to Sunda (mm/yr)					
						N	1σ	*E*	1σ	*U*	1σ
BNON	96.1508	2.5208	8.25	2010/11/29	3.08	−3.3	0.3	−20.9	0.4	−19.4	0.8
HNKO	97.3407	0.8678	106.38	2010/12/9	3.05	−2.2	0.3	−21.0	0.3	−12.9	1.3
LHW2	97.1703	1.3877	11.64	2010/12/12	2.22	8.6	0.7	−17.0	0.7	−18.1	1.7
MEGO	101.0330	−4.0102	−3.83	2012/1/11	1.79	25.6	0.8	−8.6	1.3	−34.9	3.3
PBKR	97.0828	2.0660	23.13	2011/12/30	1.24	13.3	2.0	−10.6	2.3	−6.7	9.5
PTBN	104.7822	−5.7644	25.48	2011/11/7	1.15	2.6	2.4	−8.5	3.1	−10.8	8.7
RNDG	97.8572	2.6652	−1.64	2011/11/22	2.10	0.9	0.5	−19.3	0.8	0.0	1.5
SDKL	98.1929	2.7966	889.29	2011/11/22	1.81	−1.4	0.7	−18.7	1.2	7.9	2.0

AU-SU/IN-SU convergence model that incorporates the large-scale relative motion within the Wharton Basin MORVEL [*DeMets et al*., 2010]. For the hybrid model, we assume that India-Sunda convergence occurs offshore of northernmost Sumatra and Australia-Sunda convergence occurs offshore of west Java. The plate convergence vector in the intervening areas is determined by a smooth interpolation between the India-Sunda and Australia-Sunda convergence vectors (Figure 2a). We selected 702 earthquakes from the GCMT catalog [*Ekström et al*., 2012] that are consistent with rupture of the Sunda megathrust or similarly striking thrust faults within the upper plate (thrust fault mechanisms with 60° < P1 nodal plane rake < 130°, P1 nodal plane dip < 50°, and depth < 100 km). For each event, we decompose the plate convergence velocity vector resolved at the epicentral location into the expected slip rates of faults in a simply partitioned system, using the strike of the Sunda megathrust as a proxy for the strike of the Sumatran Fault [*McCaffrey*, 1991].

The velocity components of this simple slip partitioning scheme (V_S, V_M, and V_E) are shown in Figure 6. The Australia-Sunda convergence model replicates the northward slip rate increase of over 30 mm/yr inferred by earlier studies [*McCaffrey*, 1991]. The India-Sunda convergence model predicts a lower slip rate in South Sumatra and a smaller northward increase in slip rate, attaining a maximum rate of ~15 mm/yr in northern Sumatra. The hybrid model predicts a more uniform slip rate of 16.4 ± 4.8 mm/yr (average of binned median values) along the entire Sumatran Fault between 6°S and 4°N. The initiation of the Sumatran Fault within the Sunda Strait pull apart is clearly visible for all plate convergence models as a dramatic change in V_S at around 7°S.

The trench-parallel component of velocity due to oblique slip on the Sunda megathrust (V_M) is not very sensitive to the different plate convergence models, as it mainly depends on the angle between the megathrust dip direction and the underthrusting direction (Ψ in Figure 2b) and therefore only changes a small amount when different plate convergence vectors are used. In contrast, the component of convergence velocity in the direction of earthquake slip vector azimuths (V_E), which is most relevant to the accumulation of strain due to frictional coupling of the megathrust, is highly sensitive to the plate convergence model. The hybrid convergence model integrates two important features of the India-Sunda and Australia-Sunda models: a uniform V_E of ~40 mm/yr north of the equator (from the IN-SU model), and a large gradient in V_E south of the equator (from the AU-SU model).

6. GPS Velocity Constraints on the Sumatran Fault Slip Rate

Early GPS studies of crustal deformation in Sumatra noted a significant northward increase in trench-parallel GPS velocity for fore-arc sites, interpreted as a signal of fore-arc stretching [*Prawirodirdjo et al*., 1997]. Elastic half-space models [*Savage and Burford*, 1973] of the trench-parallel component of fore-arc GPS velocity indicated a slip rate of ~30 mm/yr for the Sumatran Fault at the latitude of Toba (2.2°N) [*Prawirodirdjo et al*., 1997]. Similar slip rates of 22–26 mm/yr for the Sumatran Fault between 2°S and 4°N resulted from a similar modeling approach applied to updated campaign GPS data [*Genrich et al*., 2000]. These high slip rates appeared to be consistent with a northward increase in the Sumatran Fault slip rate, based on comparison with lower geological slip rates near the equator. Notably, these studies examined only the trench-parallel component of GPS velocity relative to Sunda as a measure of the Sumatran Fault slip rate. However, this velocity component is sensitive to both the strike-slip fault and the frictionally coupled Sunda megathrust, due to the obliquity of underthrusting beneath the fore arc. The long-term or interseismic GPS velocity of a site located on a fore-arc island is essentially the sum of near-field velocity arising from oblique elastic loading of the underlying Sunda megathrust, and far-field velocity due to elastic loading or slip on the Sumatran Fault. For sites located on the Sumatran mainland, the component of long-term trench-parallel GPS motion relative to Sunda is largely due to the Sumatran Fault, because the area of strong frictional locking of the Sunda megathrust lies well offshore.

The component of trench-parallel velocity for GPS sites located on the mainland (W_S) should therefore not greatly exceed the slip rate of the nearby segments of the Sumatran Fault (Figure 7a). Sites located relatively far west of the fault trace (>30–50 km) should integrate much of the strain or slip that is accumulated on the Sumatran Fault System, and for these sites the GPS velocity should reflect the full effects of the Sumatran Fault as well as the local oblique frictional coupling of the Sunda megathrust (Figure 7b). For these sites, the GPS velocity perpendicular to the local megathrust earthquake slip vector azimuth (W_{EQ}; calculated using the average megathrust slip vector azimuth within a 100 km radius of each site) is the full velocity component that cannot be directly attributed to megathrust coupling and is therefore a crude estimate of the slip rate of the upper plate strike-slip fault system (Figure 7a).

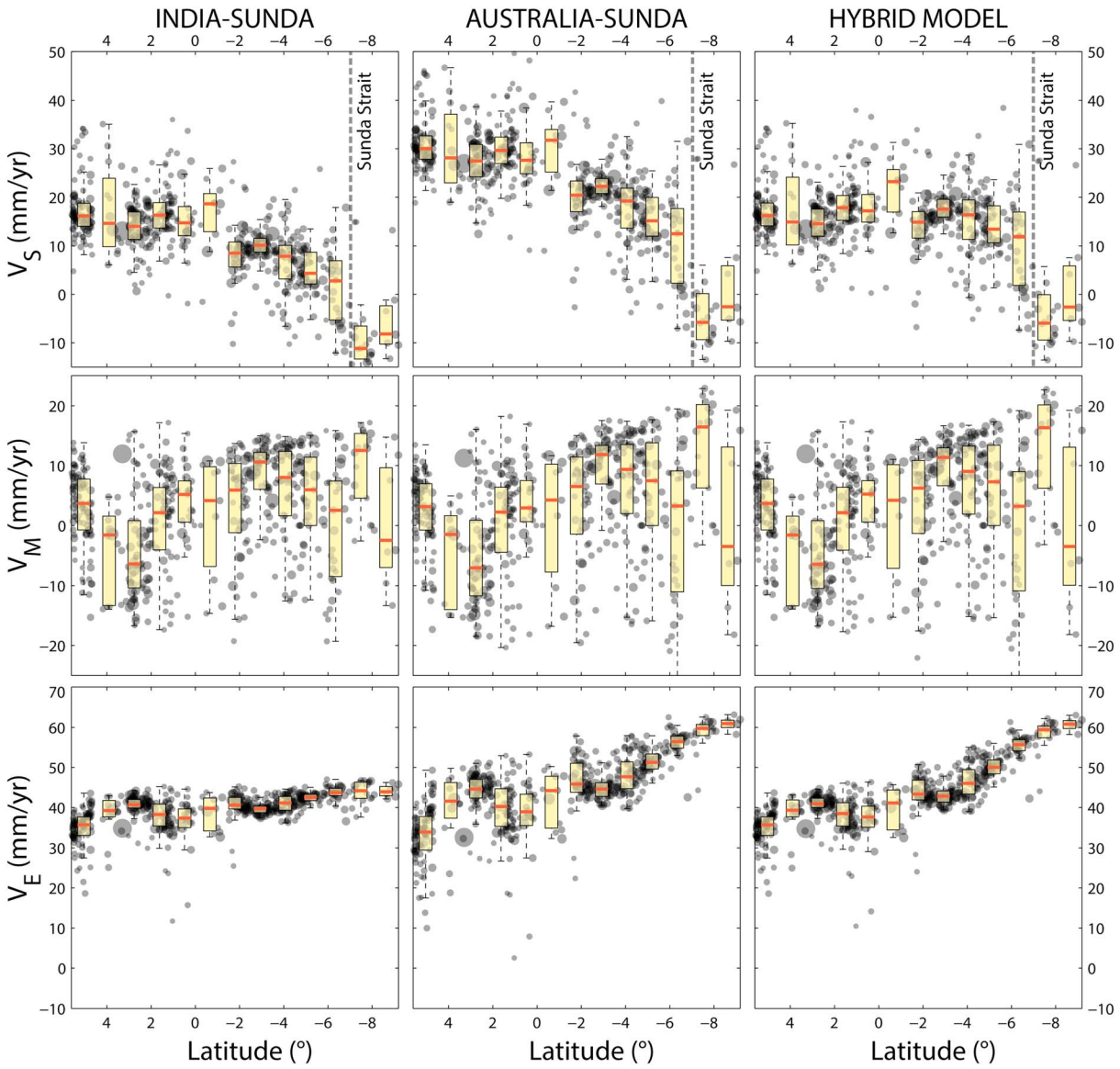

Figure 6. The latitudinal variation of partitioned components of plate convergence velocity for the Sumatran plate margin, calculated from Global Centroid Moment Tensor (GCMT) focal mechanisms for Sunda megathrust ruptures [*Ekström et al.*, 2012]. Earthquake symbols are scaled by moment magnitude. The velocity components V_S, V_M, and V_E are defined in Figure 2. In contrast with India-Sunda or Australia-Sunda convergence models, which predict a strong latitudinal variation in the strike-slip fault slip rate (V_S), the hybrid model predicts a uniform slip rate of ~15 mm/yr. The vertical dashed line in the V_S panels marks the location of the Sunda Strait, where the Sumatran Fault deviates southward toward the trench.

The component of GPS velocities for fore-arc island sites that is orthogonal to the local megathrust earthquake slip vector azimuth (W_{EQ}) varies between 10 and 20 mm/yr and clusters around 15 mm/yr (Figure 7c). Sites located south of 1°S do not exceed 16 mm/yr, while sites located north of 1°S exhibit somewhat higher W_{EQ}. Critically, two sites at Enggano exhibit very little trench-orthogonal velocity but W_{EQ} is between 15 and 17 mm/yr (notably, GPS measurements indicate subsidence and therefore some amount of megathrust coupling is likely). This strongly indicates that the Sumatran Fault slip rate is at least 15 mm/yr as far south as 5.5°S. The W_E velocities do not require significant trench-parallel elongation and are broadly consistent with a uniform Sumatran Fault slip rate along the entire Sumatran margin.

The fault-parallel GPS velocities for mainland sites (W_S) approach but do not greatly exceed 15 mm/yr, even for the most southerly sites located between 4° and 6°S (Figure 7d). For these southern sites, the component of GPS velocity orthogonal to the Sumatran Fault is small, indicating the absence of an effect on trench-perpendicular

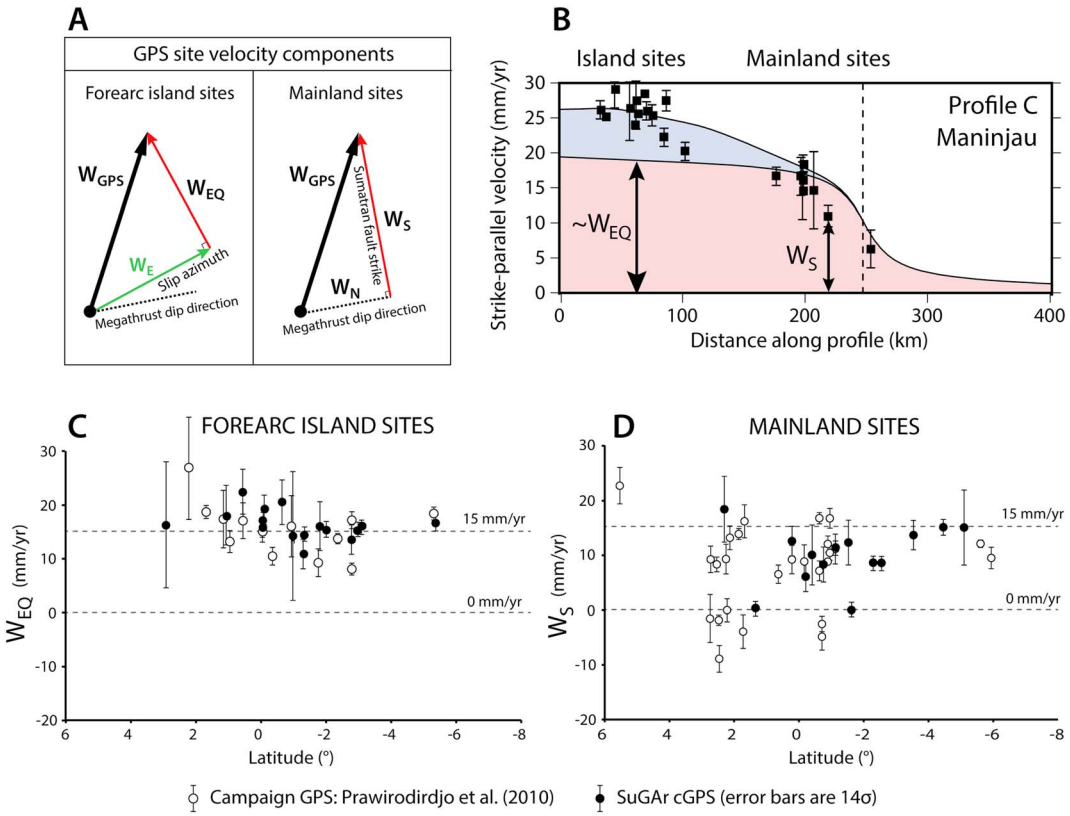

Figure 7. Long-term GPS velocities allow a simple assessment of changes in the slip rate of the Sumatran Fault with latitude, independent of the plate convergence model. (a) Components of site GPS velocities (W_{GPS}) related to the Sumatran Fault slip rate. Fore-arc island sites reflect the complete slip rate of the Sumatran Fault plus oblique frictional coupling of the underlying Sunda megathrust. Mainland sites reflect some proportion of the slip rate of the Sumatran Fault, depending on their proximity to the active fault trace. (b) Interpretation of W_{EQ} (GPS velocity orthogonal to the local megathrust slip vector azimuth) and W_S (GPS velocity parallel to the trench and the Sumatran Fault trace) for a strike-perpendicular GPS profile. Blue fill is the prediction of the full block model; pink fill is the contribution of the Sumatran Fault only. (c, d) Campaign and continuous GPS W_{EQ} and W_S velocities are broadly consistent with a 15–16 mm/yr slip rate along the entire Sumatran Fault and are inconsistent with a large northward slip rate increase.

velocity from subduction zone coupling (although continued subsidence at Enggano does indicate frictional coupling). The sites with velocities of ~0 mm/yr are located on Sunda far from the Sumatran Fault. The SuGAr GPS sites are mostly located along the coastline, between 24 and 66 km (average of 40 km) from the trace of the Sumatran Fault and should therefore capture much of the strain accumulated by that structure. Because the W_S velocities approach but do not significantly exceed ~15 mm/yr from southernmost to northernmost Sumatra, we conclude that the slip rate of the Sumatran Fault System is not much higher than ~15–16 mm/yr.

7. Kinematic Block Model of Slip Partitioning

We evaluate the relationship between relative motion within the Wharton Basin, the newly revised geological slip rates of the Sumatran Fault, and coupling on the megathrust using a heterogeneously coupled elastic block model implemented in DEFNODE [*McCaffrey*, 2002]. This model is similar in most aspects to previously published models of Sumatra using the same code and modeling approach [*McCaffrey*, 2002; *Prawirodirdjo et al*., 2010]. The Sumatran Fault is described by 28 nodes at depths of 0 km, 15 km, and 20 km, approximating the main Sumatran Fault segments and their offshore extensions in the Sunda Strait and the southern Andaman Sea. The coupling on the Sumatran Fault is allowed to vary laterally, with the nodes at 0 and 15 km depth at a given location being constrained to have the same value of the locking coefficient ϕ (locked fault slip divided by total slip) in the inversion, and nodes at 20 km depth being set to $\phi = 0$ (uncoupled). The Sunda megathrust is described using six node depths (5, 13, 25, 50, 75, and 100 km), with the 100 km depth nodes placed beneath the Sumatran Fault (nearly equivalent to the magmatic arc) and set to $\phi = 0$, the 5 km depth nodes placed at the trench, and the intermediate nodes placed at positions that approximate the

location of the megathrust. This megathrust geometry is similar to previous studies [*Prawirodirdjo et al*., 2010]; however, we took care to ensure that the strike of the megathrust locally agrees with the average strike of the nodal planes of the megathrust earthquakes used in this study. We simulate distributed lithospheric deformation within the Wharton Basin by subdividing the slab into three rigid blocks separated by freely slipping vertical strike-slip faults ($\phi = 0$ for all nodes) that approximately follow small circle paths centered on the MORVEL AU-SU and IN-SU poles of relative rotation, thereby minimizing across-fault motion. These faults intersect the megathrust and extend to 100 km depth, but do not cut the fore-arc block. The degree of localized deformation within the subducting slab is limited by constraining slip rates on these hypothetical faults to be less than 7 mm/yr, preventing artificially large steps in the velocity of subduction along the trench. It is important to note that the relative motion of the oceanic blocks is only well defined in the areas where they extend beneath the fore arc and slip vector data are available and that the model is not sensitive to the location or orientation of the hypothetical faults separating the blocks within the Wharton Basin. We simultaneously estimate the angular velocities of the three oceanic blocks and the fore-arc sliver block relative to Sunda (Table 2), as well as the laterally variable coupling of the upper 15 km of the Sumatran Fault and the spatially heterogeneous coupling of the Sunda megathrust.

We constrain the kinematic block model GPS site velocities, Sunda megathrust earthquake slip vector azimuths derived from Global Centroid Moment Tensor solutions [*Ekström et al*., 2012], and Sumatran Fault strikes for segments that show geomorphic and seismic evidence for purely strike-slip offset [*Sieh and Natawidjaja*, 2000]. We also include two GPS velocities for the Christmas and Cocos islands relative to Sunda [*Hanifa et al*., 2014] that constrain the overall plate convergence offshore of Java. While coral uplift data can significantly improve the constraints on the detailed pattern of megathrust coupling over the 50 years prior to the great 2004 earthquake [*Philibosian et al*., 2014], our tests indicate that the inferred block motions are not sensitive to these data. In an effort to match the epochs of the observational data as closely as possible, we elect to not include the coral uplift data in the model.

In order to test whether our approach is biased by long-lasting effects of the cascade of great earthquakes that have occurred on the Sunda megathrust since 2004, we implemented two models that incorporate different GPS velocity data. One model utilizes the new SuGAr long-term GPS velocities (Table 1), while the second utilizes the available campaign mode GPS velocities [*Prawirodirdjo et al*., 2010]. The analytical uncertainties of all data were multiplied by weight factors designed to achieve even weighting in the inversion while respecting the magnitude of observed variation within each data set. The GCMT slip vector azimuths and Sumatran Fault strike directions are assigned an uncertainty of 5°. We exclude sites from the SuGAr network with short observation periods that exhibit strong trenchward motion and are unlikely to represent long-term strain accumulation or show anomalous velocities compared to velocity trends from nearby sites (Table 2). We multiply the estimated uncertainties of the SuGAr site velocities by a factor of 14 and the site velocities of the Christmas and Cocos Islands [*Hanifa et al*., 2014] by a factor of 8, reflecting the fact that the stated uncertainties of the continuous GPS velocities are very small compared to the between-site velocity variation and the uncertainties of the campaign GPS data.

We observe good agreement between the two models, reflecting the general similarity of the continuous GPS velocity field with earlier campaign GPS velocities. The pattern of long-term strain accumulation in the Sumatran fore arc is explained well by rigid block rotation and heterogeneous frictional coupling on the Sunda megathrust and Sumatran Fault (Figure 8). Like previous studies, we infer strong coupling of the Sunda megathrust beneath most fore-arc islands, weak coupling beneath the Batu Islands, and very weak coupling south of 4°S [*Chlieh et al*., 2008; *Prawirodirdjo et al*., 2010]. In contrast with previous models that assumed a rigid oceanic plate, we attain a good fit to megathrust slip vector azimuths along the entire Sumatran margin. The plate convergence velocity fields of the northern and southern oceanic blocks with respect to Sunda are similar to the fields derived from MORVEL Australia-Sunda and India-Sunda angular velocities [*DeMets et al*., 2010], and the inferred rate of trench-parallel shortening of the Wharton Basin oceanic lithosphere over the entire Sumatran margin is consistent with the observed relative motion of GPS sites located in India and Australia [*Delescluse and Chamot-Rooke*, 2007]. The models therefore sufficiently account for the overall amount of internal deformation of the Wharton Basin lithosphere, if not its detailed distribution.

The poles of rotation describing relative plate motion for the five-block model constrained by SuGAr GPS data are presented in Table 3. While these pole locations are not tightly constrained due to the narrow aperture of

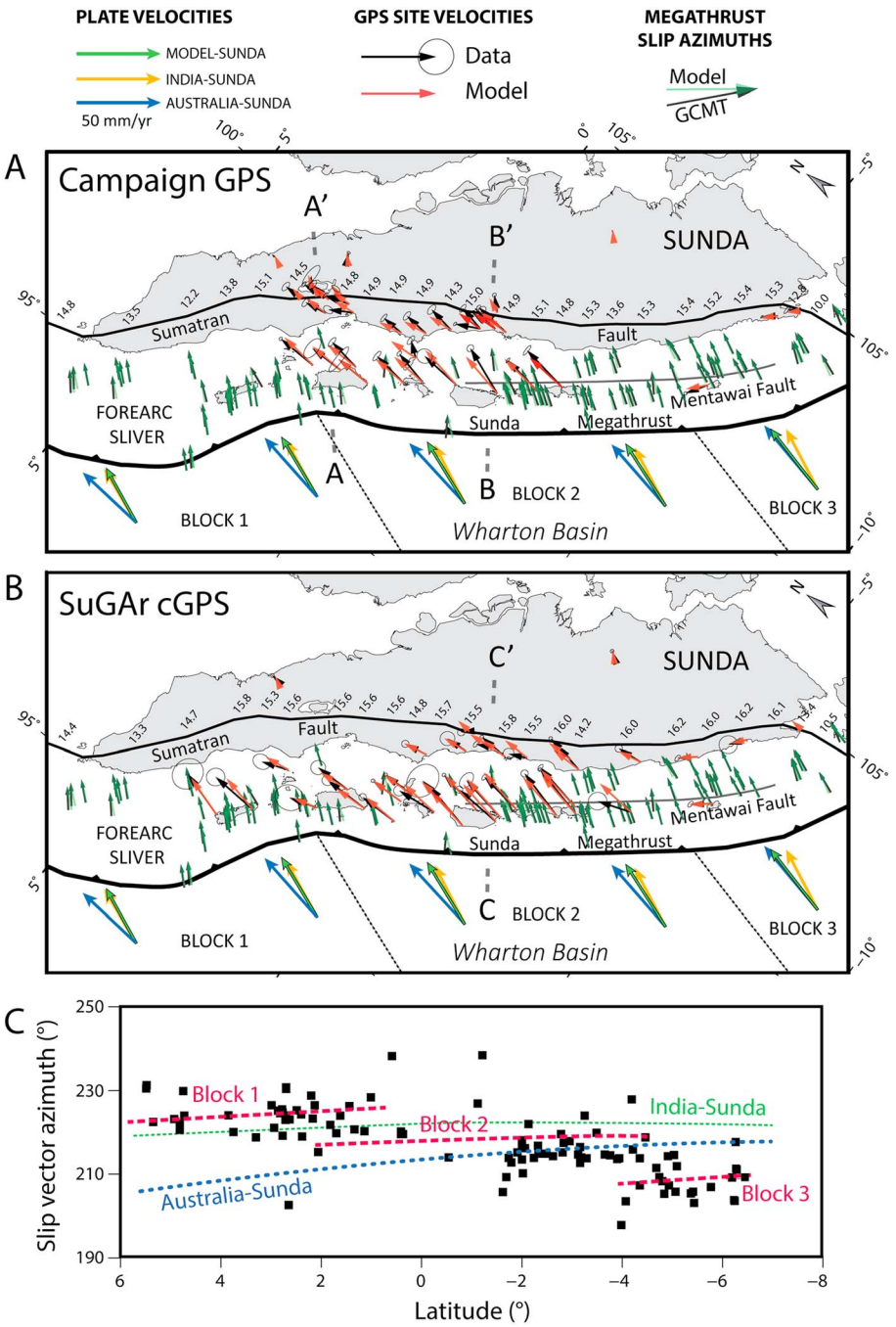

Figure 8. Kinematic block models of slip partitioning in Sumatra that simulate internal deformation of the Wharton Basin lithosphere using three independent oceanic blocks separated by uncoupled (freely slipping) vertical faults. The three oceanic blocks extend beneath the single fore-arc block. Data are adequately explained by heterogeneous coupling on the Sunda megathrust beneath a rigid fore-arc block that is separated from Sunda by the Sumatran Fault that slips at an average rate of 15–16 mm/yr. GPS profiles A-A′, B-B′, and C-C′ are plotted in Figure 10. (a) Block model using campaign GPS of *Prawirodirdjo et al.* [2010]. (b) Block model using SuGAr continuous GPS presented in this paper. (c) The piecewise fit of megathrust slip vector azimuths from the block model improves on the significant misfits of the Australia-Sunda and India-Sunda plate motion models.

slip vector data defining the relative motion of each block, the general consistency with MORVEL Australia-Sunda and India-Sunda plate motion (Figure 9) indicates that the block model adequately encompasses the broad deformation across the Wharton Basin due to India-Australia convergence. The pole of rotation of the sliver block relative to Sunda is located within the South China Sea, in contrast with a pole position located offshore of South Africa that was estimated solely from the geometry of the Sumatran Fault [*Chlieh et al.*, 2008].

Table 3. Poles of Rotation Describing Plate Motions Relative to Sunda for the Five-Block Model Constrained by SuGAr GPS Data

Pole of Rotation	Latitude	Longitude	Rotation Rate (°/Myr)
Block 1-Sunda	20.52	47.40	0.56
Block 2-Sunda	20.12	31.69	0.57
Block 3-Sunda	4.88	63.22	0.85
Sliver-Sunda	11.83	117.083	−0.40

Notably, our new pole position is consistent with margin-parallel transport of a long, curved sliver plate stretching from West Java to southern Myanmar, while the rotation pole of *Chlieh et al.* [2008] would require breakup of the sliver plate in North Sumatra.

For both the SuGAr and campaign GPS models, the estimated slip rate for purely strike-slip segments of the Sumatran Fault varies between 14 and 16 mm/yr, with locally lower rates that coincide with restraining or releasing bends where significant across-fault motion is expected. This result agrees with a previous slip rate estimate for central Sumatra of ~14 mm/yr [*McCaffrey*, 2002], which was difficult to reconcile with the geological and geodetic slip rates then available. Earlier geodetic studies that inferred between 21 and 30 mm/yr Sumatran Fault slip rates in North Sumatra [*Prawirodirdjo et al.*, 1997; *Genrich et al.*, 2000] appear to have significantly underestimated the degree of trench-parallel motion of the fore-arc islands arising from oblique loading of the Sunda megathrust. These studies assumed that the trench-parallel component of GPS motion was dominated by the effect of the Sumatran Fault and estimated the slip rate of the Sumatran Fault by fitting the trench-parallel component of GPS velocity profiles crossing the entire fore arc to a single strike-slip fault (Figure 10). The inferred slip rates coincidentally matched the high geological slip rates then available for the Renun segment [*Sieh and Natawidjaja*, 2000; *Detourbet et al.*, 1993], which we have revised downward in this study.

8. Discussion

8.1. Kinematics of Slip Partitioning

The transition from Australia-Sunda to India-Sunda convergence along the Sumatran margin due to internal deformation of the Wharton Basin oceanic lithosphere results in a northward decrease in total plate convergence velocity from 65 to 45 mm/yr, an eastward rotation by 15° of the convergence vector relative to Sunda, and a nearly uniform obliquity of underthrusting beneath the fore arc of 20°. Despite the strong curvature of

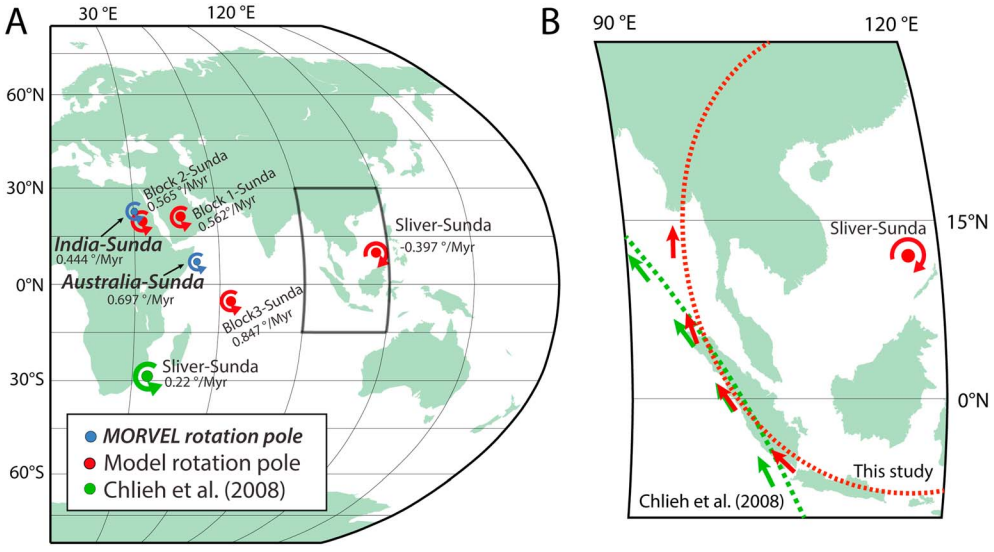

Figure 9. Poles of relative rotation for the plate convergence models discussed in this study. (a) Comparison of poles inferred by the five-block model with MORVEL poles [*DeMets et al.*, 2010] and a pole describing the motion of the fore arc relative to Sunda (sliver-Sunda) from *Chlieh et al.* [2008]. Model rotation poles are for the five-block model constrained by SuGAr GPS data. (b) A sliver-Sunda pole of rotation located in the Philippine Sea is compatible with transport of a long fore-arc block along the curved Sumatran margin.

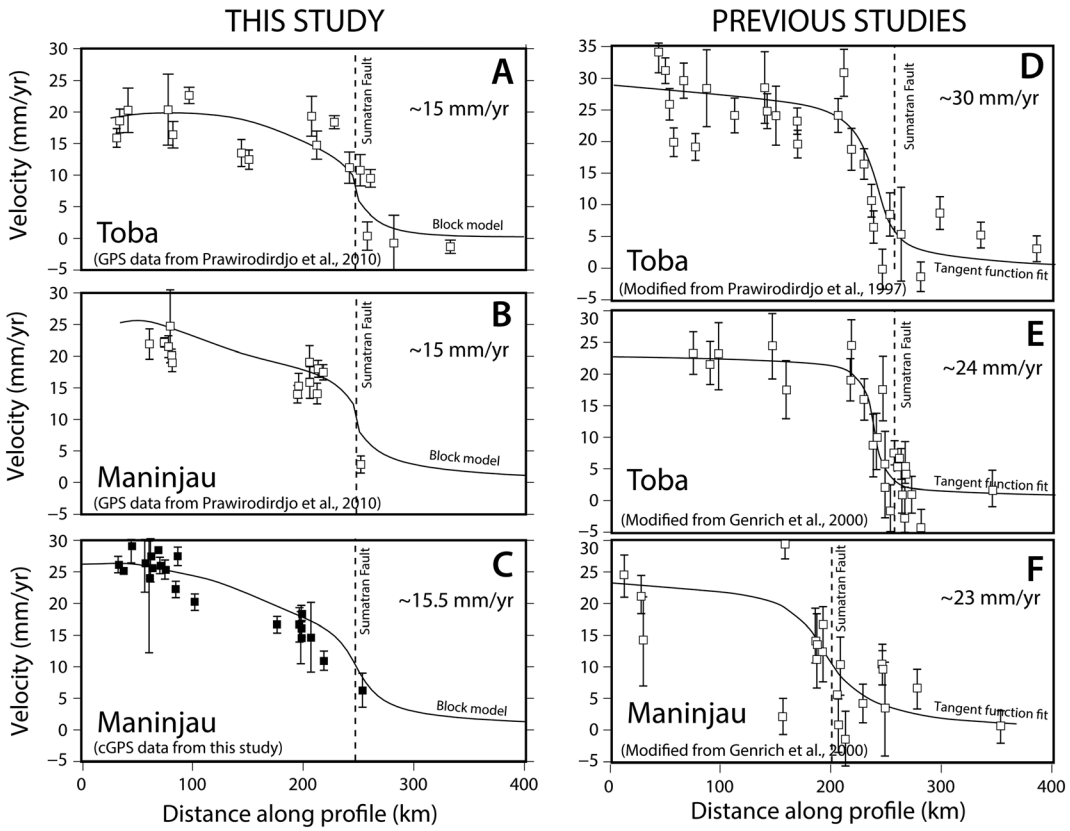

Figure 10. Comparison of GPS velocity profiles across the Sumatran fore arc inferred from (left) kinematic block models (right) with previously published velocity profiles. Modeling all fore-arc site velocities with a single strike-slip fault results in anomalously high inferred slip rates (>22 mm/yr) and mislocation of the Sumatran Fault trace by up to 40 km. Incorporating the effect of oblique locking of the Sunda megathrust results in lower inferred slip rates for the Sumatran Fault (~15 mm/yr) that are more consistent with updated geological slip rates.

the margin, the resulting plate motion vector field neither strongly converges nor diverges beneath the Sumatran fore arc, allowing effectively rigid translation of the mobile fore-arc block relative to Sunda [*McCaffrey*, 1992; *Platt*, 2000].

The observed 15 mm/yr geological and geodetic slip rates of the Sumatran Fault (Figure 11) are consistent with both the regional block model (which assumes a rigid fore-arc block) and the local frictional balance model (which allows the fore arc to deform internally). The close agreement between geological slip rates and the slip rates estimated from these models indicates that the full budget of oblique convergence along the Sumatran margin is accommodated by oblique slip on the Sunda megathrust and strike-slip motion of the Sumatran Fault Zone. Studies of the frictional coupling on the megathrust that incorrectly account for this fore-arc motion (e.g., the 23 mm/yr Sumatran fault slip rate assumed by *Chlieh et al*. [2008]) will exhibit a systematic bias in the strength of coupling due to the direct trade-off between the trench-parallel velocity of the fore-arc sliver and the strength of coupling inferred from GPS velocities.

Slip partitioning controls the obliquity of underthrusting beneath the fore-arc wedge (Ψ) and the obliquity of plate convergence (γ) (see Figure 2 for the definition of these angles). Where subduction zones are obliquely convergent but not partitioned, $\Psi = \gamma$ and slip vector azimuths are parallel to the local plate convergence direction. Where decoupling is complete, $\Psi = 0$ and trench-parallel convergence is completely accommodated by the upper plate strike-slip fault. Assuming a uniform plate convergence azimuth of 003°, *McCaffrey* [1992] proposed that binned earthquake data from Sumatra are consistent with an onset of slip partitioning at a critical convergence obliquity of ~20° and that the underthrusting obliquity attains a maximum value (Ψ_{max}) between 15 and 25°. A plot of Ψ versus γ from GCMT focal mechanisms of fore-arc thrust earthquakes that occurred between 1976 and 2013 shows a significantly different pattern (Figure 12). We

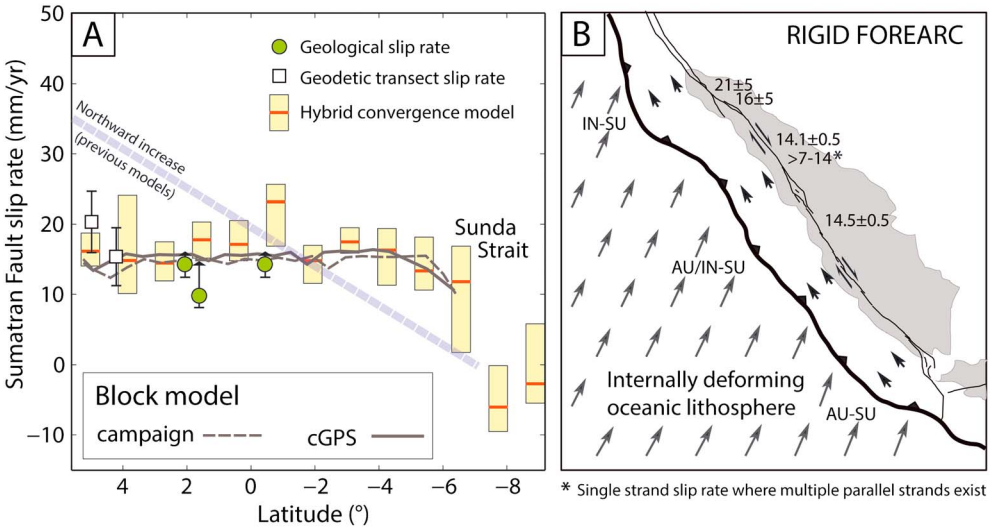

Figure 11. (a) Comparison of reliable Sumatran Fault geological slip rates [*Hickman et al.*, 2004; *Ito et al.*, 2012; this study] with the predicted slip rate variation estimated from block modeling and a local frictional balance model. The geological and geodetic slip rates are most compatible with a uniform slip rate model, implying that the Sumatran fore arc has not undergone significant trench-parallel stretching during at least the last 100 kyr. (b) Map view of plate convergence vectors derived from a five-block model and reliable Sumatran Fault slip rate estimates. Note the lack of convergence or divergence near the trench of the velocity field of the oceanic lithosphere relative to Sunda.

estimate the slab dip direction and slip vector azimuth from each focal mechanism and calculate the plate convergence direction using the previously discussed hybrid model that smoothly transitions from Australia-Sunda to India-Sunda plate motion (Figure 2a). The scatter of Ψ arises primarily from local variations in the dip direction of the Sunda megathrust. Most Sumatran earthquakes with $\Psi < 0°$ occur between 2 and 4°N, where the strike of the megathrust rotates westward and the sense of underthrusting obliquity reverses.

Earthquakes from the Java fore-arc fall near the $\Psi = \gamma$ line, indicating a lack of slip partitioning along this part of the margin where convergence is nearly normal. Interestingly, some earthquakes have $\Psi > \gamma$, indicating that underthrusting is less oblique than plate convergence. This could be evidence for a component of left-lateral strike-slip motion of the Java fore arc relative to Sunda, possibly accommodated by active slip along the Cimandiri-Lembang-Baribis fault system [*Abidin et al.*, 2009]. Earthquakes from the Sumatran fore arc define a linear trend with a slope of 1 that is shifted from the $\Psi = \gamma$ trend. This shift can be explained by rigid motion of a fore-arc sliver, which would not affect the plate convergence direction or the slab dip (or, therefore, γ) but would reduce Ψ by a similar value for all earthquakes. The ~18° shift in Ψ is consistent with an average velocity of the fore-arc block relative to Sunda of ~16 mm/yr, and the clear separation between Sumatra and Java fore-arc earthquakes points to a sudden initiation of slip partitioning within the Sunda Strait. In contrast with previous interpretations, we find that Ψ does not attain a clear maximum value, and nowhere along the Sumatran margin does $\Psi = \gamma$.

8.2. Fore-Arc Rheology and Fault Strength

The existence of a rigid fore-arc block separated from Sunda by a plate boundary transform fault has broad implications on how we understand the active tectonics of the Sumatran margin as well as its overall tectonic evolution. Previous interpretations of trench-parallel fore-arc stretching or broadly distributed fore-arc transpression [*McCaffrey*, 1992; *Tikoff and Teyssier*, 1994] inferred that a significant amount of the strain accumulated on the Sunda megathrust was released by permanent and diffuse upper plate deformation. This would effectively reduce the long-term rate of seismic moment release by megathrust earthquakes. In the absence of geological evidence for widespread permanent deformation of the fore-arc crust, we instead infer that the elastic strain accumulated within the fore-arc crust during the earthquake cycle is ultimately released by rupture of the megathrust.

Because the Sunda megathrust and Sumatran Fault together accommodate nearly the full budget of oblique plate convergence, the Mentawai Fault and other steeply dipping, trench-parallel fore-arc faults do not have

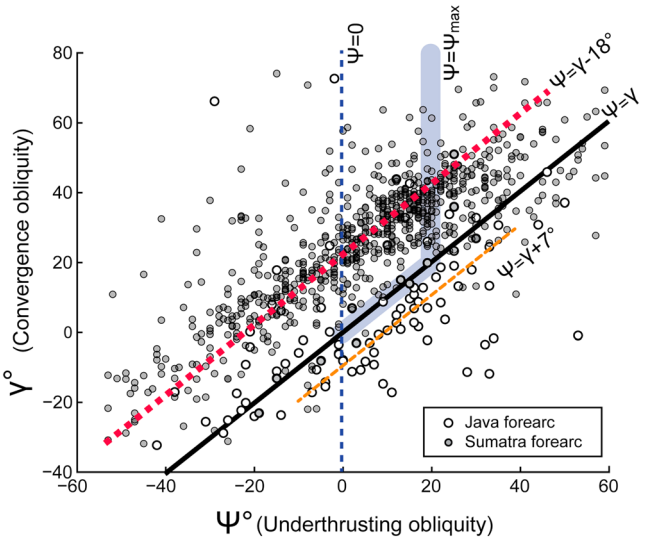

Figure 12. The relationship between convergence obliquity (γ) and underthrusting obliquity (Ψ) in Sumatra, estimated from GCMT focal mechanisms and an assumed hybrid plate model that accounts for Australia-India convergence (Figure 2a). $\Psi = 0$: theoretical trend for a completely decoupled margin. $\Psi = \gamma$: theoretical trend for a completely coupled margin with no slip partitioning and no scatter in Ψ due to structural complexity of the megathrust. $\Psi = \Psi_{max}$: trend proposed by *McCaffrey* [1992] for Sumatra based on binned earthquake data, suggesting a physical limit on underthrusting obliquity. $\Psi = \gamma - 18°$: general trend of Sumatran fore-arc earthquakes that is consistent with an obliquely coupled megathrust and trench-parallel motion of a rigid fore-arc sliver block. $\Psi = \gamma + 7°$: general trend of Java fore-arc earthquakes that may arise from active left-lateral strike-slip faulting in Java.

a large budget for active strike-slip motion. These faults are best interpreted as high-angle reverse faults that developed during construction of the accretionary wedge [*Singh et al.*, 2010; *Wiseman et al.*, 2011], and not as active strike-slip faults [*Diament et al.*, 1992].

Previous force balance analyses assumed that the lower plate does not deform, except by bending at the slab hinge zone and that the degree of slip partitioning (as reflected in a critical obliquity of underthrusting beneath the fore arc) therefore reflects the relative frictional properties of the subduction megathrust and the upper plate strike-slip fault [*McCaffrey*, 1992; *Platt*, 2000]. However, the clear evidence for internal shortening of the Wharton Basin lithosphere and the lack of clear evidence for stretching of the Sumatran fore arc indicate that lower plate deformation is a dominant factor in this slip partitioning system.

If the distributed internal deformation of the Wharton Basin lithosphere is driven purely by far-field stresses transmitted from the Indian collision zone and the Banda subducting slab [*Cloetingh and Wortel*, 1985; *Delescluse et al.*, 2012; *Gordon and Houseman*, 2015], then it is simply a coincidence that the forces imposed on the base of the Sumatran fore arc closely match the primary condition for the existence of a coherent fore-arc block: a low degree of divergence of the direction of frictional underthrusting. In this scenario, the base of the fore arc is not subjected to a strong lateral stress gradient, and the sliver can be viewed either as a rigid block or as a plastic wedge that would deform internally if only it were properly stressed. The ~15–16 mm/yr slip rate of the Sumatran Fault is then a product of regional plate motions and does not reflect a limiting mechanical property of the slip partitioning system. Alternatively, if mechanical interactions of the slip partitioning system work to reduce the divergence of plate convergence velocity vectors beneath the fore arc, then lateral stresses are imposed on the subducting slab through frictional megathrust coupling at the base of the fore arc that help drive compressive deformation of the lower plate. This mechanism could explain why the strongest internal deformation of the Wharton Basin, as evidenced by seismicity as well as regional deformation modeling [*Gordon and Houseman*, 2015] coincides with the area just offshore of the mobile Sumatran fore arc (Figure 2). In this study, we adopted a simplified description of the overall kinematics in order to better understand the deformation of the Sumatran fore arc; it is likely that a more complex modeling approach that incorporates more realistic geological structures that are consistent with the seismicity and long-term deformation of the Wharton Basin oceanic lithosphere will be required to better understand the physical mechanisms that link slip partitioning and diffuse intraplate deformation.

9. Conclusions

Geological slip rate measurements from the Sumatran Fault, geodetic measurements of fore-arc deformation during the last seismic cycle, and regional plate motions are all consistent with a rigid fore-arc sliver block separated from Sunda by the Sumatran Fault. This plate boundary fault system accumulates dextral strike-slip

displacement at an average rate of ~15–16 mm/yr along much of its length. Geodetic measurements of fore-arc strain accumulation indicate that oblique underthrusting beneath the fore arc contributes up to 40% of the trench-parallel component of interseismic GPS velocity. Slip partitioning in Sumatra represents an interplay between not only the frictional properties of the Sumatran Fault and the Sunda megathrust (and the rheology of the fore-arc crust) but also the complex and poorly understood set of active high-angle faults within the downgoing plate (and the rheology of the Wharton Basin oceanic lithosphere).

Acknowledgments

Daily RINEX files of the SuGAr GPS data used in this study are available for public download at ftp://eos.ntu.edu.sg/SugarData. Early data are also archived at the Scripps Orbit and Permanent Array Center (SOPAC). We are grateful to the scientists and field technicians who keep the SuGAr network in operation, including P. Banerjee, J. Galetzka, J. Encillo, I. Suprihanto, D. Prayudi, Iwan Hermawan, and B. Suwargadi. We also thank Mudrik R. Daryono for interesting discussions in the field. GMT [*Wessel et al*., 2013] was used to produce several figures. This research was supported by the Earth Observatory of Singapore via its funding from the National Research Foundation Singapore and the Singapore Ministry of Education, under the Research Centres of Excellence program, and by the National Research Foundation Singapore under its Singapore NRF Fellowship scheme (National Research Fellow Award NRF-NRFF2010-064). This work comprises Earth Observatory of Singapore contribution 139.

References

Abidin, H. Z., H. Andreas, T. Kato, T. Ito, I. Meilano, F. Kimata, D. H. Natawidjaja, and H. Harjono (2009), Crustal deformation studies in Java (Indonesia) using GPS, *J. Earthq. Tsunami*, *03*(02), 77–88.

Abercrombie, R. E., M. Antolik, and G. Ekström (2003), The June 2000 M_w 7.9 earthquakes south of Sumatra: Deformation in the India–Australia Plate, *J. Geophys. Res.*, *108* 2018, doi:10.1029/2001JB000674.

Alloway, B. V., A. Pribadi, J. A. Westgate, M. Bird, L. Keith Fifiel, A. Hogg, and I. Smith (2004), Correspondence between glass-FT and 14 C ages of silicic pyroclastic flow deposits sourced from Maninjau caldera, west-central Sumatra, *Earth Planet. Sci. Lett.*, *227*, 121–133.

Altamimi, Z., L. Métivier, and X. Collilieux (2012), ITRF2008 plate motion model, *J. Geophys. Res.*, *117*, B07402, doi:10.1029/2011JB008930.

Andrade, V., and K. Rajendran (2014), The April 2012 Indian Ocean earthquakes: Seismotectonic context and implications for their mechanisms, *Tectonophysics*, *617*, 126–139.

Ascough, P. L., M. I. Bird, F. Brock, T. F. G. Higham, W. Meredith, C. E. Snape, and C. H. Vane (2009), Hydropyrolysis as a new tool for radiocarbon pre-treatment and the quantification of black carbon, *Quat. Geochronol.*, *4*(2), 140–147.

Bellier, O., M. Sebrier, and S. Pramumijoyo (1991), The Great Sumatran Fault—Geometry, kinematics and offset, analysed by satellite imagery, *C. R. Acad. Sci. Paris Sér. I Math*, *312*, 1219–1226.

Bellier, O., and M. Sébrier (1994), Relationship between tectonism and volcanism along the Great Sumatran fault zone deduced by SPOT image analyses, *Tectonophysics*, *233*(3), 215–231.

Bellier, O., H. Bellon, M. Sébrier, and R. C. Maury (1999), K–Ar age of the Ranau Tuffs: Implications for the Ranau caldera emplacement and slip-partitioning in Sumatra (Indonesia), *Tectonophysics*, *312*(2), 347–359.

Bellier, O., and M. Sébrier (1995), Is the slip rate variation on the Great Sumatran Fault accommodated by fore-arc stretching?, *Geophys. Res. Lett.*, *22*, 1969–1972, doi:10.1029/95GL01793.

Bennett, J. D., et al. (1981), *Geologic Map of Banda Aceh Quadrangle, North Sumatra, 1:250000*, Geol. Res. and Dev. Cent, Bandung, Indonesia.

Chesner, C., W. I. Rose, A. L. Deino, R. Drake, and J. A. Westgate (1991), Eruptive history of Earth's largest Quaternary caldera (Toba, Indonesia) clarified, *Geology*, *19*(3), 200–203.

Chlieh, M., J.-P. Avouac, K. Sieh, D. H. Natawidjaja, and J. Galetzka (2008), Heterogeneous coupling of the Sumatran megathrust constrained by geodetic and paleogeodetic measurements, *J. Geophys. Res.*, *113* B05305, doi:10.1029/2007JB004981.

Cloetingh, S., and R. Wortel (1985), Regional stress field of the Indian plate, *Geophys. Res. Lett.*, *12*, 7–80, doi:10.1029/GL012i002p00077.

Delescluse, M., and N. Chamot-Rooke (2007), Instantaneous deformation and kinematics of the India–Australia Plate, *Geophys. J. Int*, *168*, 818–842.

Delescluse, M., N. Chamot-Rooke, R. Cattin, L. Fleitout, O. Trubienko, and C. Vigny (2012), April 2012 intra-oceanic seismicity off Sumatra boosted by the Banda-Aceh megathrust, *Nature*, *490*(7419), 240–244.

DeMets, C., R. Gordon, and D. Argus (2010), Geologically current plate motions, *Geophys. J. Int*, *181*, 1–80.

Deplus, C., M. Diament, H. Hébert, G. Bertrand, S. Dominguez, J. Dubois, J. Malod, P. Patriat, B. Pontoise, and J. Sibilla (1998), Direct evidence of active deformation in the eastern Indian oceanic plate, *Geology*, *26*(2), 131–134.

Detourbet, C., O. Bellier, and M. Sébrier (1993), La caldera volcanique de Toba et filesysteme de faille de Sumatra (Indonesia) vue par SPOT, *C. R. Acad. Sci., Ser. II*, *316*, 1439–1445.

Diament, M., H. Harjono, K. Karta, C. Deplus, D. Dahrin, M. T. Zen, G. Lassal, A. Martin, and J. Malod (1992), Mentawai fault zone off Sumatra: A new key to the geodynamics of western Indonesia, *Geology*, *20*, 259–262.

Ekström, G., M. Nettles, and A. M. Dziewonski (2012), The global CMT project 2004–2010: Centroid-moment tensors for 13,017 earthquakes, *Phys. Earth Planet. Inter.*, *200–201*, 1–9.

Fauzi, R. M., R. McCaffrey, D. Wark, P. Y. Prih Haryadi, and Sunarjo (1996), Lateral variation in slab orientation beneath Toba caldera, northern Sumatra, *Geophys. Res. Lett.*, *23*, 443–446, doi:10.1029/96GL00381.

Feng, L., E. M. Hill, P. Banerjee, I. Hermawan, L. L. H. Tsang, D. H. Natawidjaja, B. W. Suwargadi, and K. Sieh (2015), A unified GPS-based earthquake catalog for the Sumatran plate boundary between 2002 and 2013, *J. Geophys. Res. Solid Earth*, *120*, 3566–3598, doi:10.1002/2014JB011661.

Fitch, T. J. (1972), Plate convergence, transcurrent faults, and internal deformation adjacent to southeast Asia and the western Pacific, *J. Geophys. Res.*, *77*, 4432–4460, doi:10.1029/JB077i023p04432.

Genrich, J. F., Y. Bock, R. McCaffrey, L. Prawirodirdjo, C. W. Stevens, S. S. O. Puntodewo, C. Subarya, and S. Wdowinski (2000), Distribution of slip at the northern Sumatran fault system, *J. Geophys. Res.*, *105*, 28,327–28,341, doi:10.1029/2000JB900158.

Gordon, R. G., C. DeMets, and D. F. Argus (1990), Kinematic constraints on distributed lithospheric deformation in the equatorial Indian Ocean from present motion between the Australian and Indian plates, *Tectonics*, *9*, 409–422, doi:10.1029/TC009i003p00409.

Gordon, R. G., and G. A. Houseman (2015), Deformation of Indian Ocean lithosphere: Evidence for a highly nonlinear rheological law, *J. Geophys. Res. Solid Earth*, *120*, 4434–4449, doi:10.1002/2015JB011993.

Hanifa, N. R., T. Sagiya, F. Kimata, J. Efendi, H. Z. Abidin, and I. Meilano (2014), Interplate coupling model off the southwestern coast of Java, Indonesia, based on continuous GPS data in 2008–2010, *Earth Planet. Sci. Lett.*, *401*, 159–171.

Hickman, R. G., P. F. Dobson, M. van Gerven, B. D. Sagala, and R. P. Gunderson (2004), Tectonic and stratigraphic evolution of the Sarulla graben geothermal area, North Sumatra, Indonesia, *J. Asian Earth Sci.*, *2004*(23), 435–448, doi:10.1016/S1367-9120(03)00155-X.

Hill, E. M., et al. (2015), The 2012 M_w 8.6 Wharton Basin sequence: A cascade of great earthquakes generated by near-orthogonal, young, oceanic mantle faults, *J. Geophys. Res. Solid Earth*, *120*, 3723–3747, doi:10.1002/2014JB011703.

Ishii, M., E. Kiser, and E. L. Geist (2013), M_w 8.6 Sumatran earthquake of 11 April 2012: Rare seaward expression of oblique subduction, *Geology*, *41*, 319–322.

Ito, T., E. Gunawan, F. Kimata, T. Tabei, M. Simons, I. Meilano, Y. Ohta, I. Nurdin, and D. Sugiyanto (2012), Isolating along-strike variations in the depth extent of shallow creep and fault locking on the northern Great Sumatran Fault, *J. Geophys. Res.*, *117* B06409, doi:10.1029/2011JB008940.

Jarrard, R. D. (1986), Terrane motion by strike-slip faulting of forearc slivers, *Geology*, *14*, 780–783.
Manville, V., K. Németh, and K. Kano (2009), Source to sink: A review of three decades of progress in the understanding of volcaniclastic processes, deposits, and hazards, *Sediment. Geol.*, *220*(3), 136–161.
Mark, D. F., M. Petraglia, V. Smith, L. Morgan, D. Barfod, B. Ellis, N. Pearce, J. N. Pal, and R. Korisettar (2014), A high-precision $^{40}Ar/^{39}Ar$ age for the Young Toba Tuff and dating of ultra-distal tephra: Forcing of Quaternary climate and implications for hominin occupation of India, *Quat. Geochronol.*, *21*, 90–103.
McCaffrey, R. (1991), Slip vectors and stretching of the Sumatran fore arc, *Geology*, *19*, 881–884.
McCaffrey, R. (1992), Oblique plate convergence, slip vectors, and forearc deformation, *J. Geophys. Res.*, *97*, 8905–8915, doi:10.1029/92JB00483.
McCaffrey, R. (1994), Global variability in subduction thrust zone-forearc systems, *Pure Appl. Geophys.*, *142*(1), 173–224.
McCaffrey, R., P. C. Zwick, Y. Bock, L. Prawirodirdjo, J. F. Genrich, C. W. Stevens, S. S. O. Puntodewo, and C. Subarya (2000), Strain partitioning during oblique plate convergence in northern Sumatra: Geodetic and seismologic constraints and numerical modelling, *J. Geophys. Res.*, *105*, 28,363–28,376, doi:10.1029/1999JB900362.
McCaffrey, R. (2002), Crustal block rotations and plate coupling, in *Plate Boundary Zones*, *AGU Geodynamics Series 30*, edited by S. Stein and J. Freymueller, pp. 101–122, AGU, Washington, D. C.
Mckenzie, D. P., and R. L. Parker (1967), The North Pacific: An example of tectonics on a sphere, *Nature*, *216*, 1276–1280.
Ninkovich, D., N. J. Shackleton, A. A. Abdel-Monem, J. D. Obradovich, and G. Izett (1978), K–Ar age of the late Pleistocene eruption of Toba, north Sumatra, *Nature*, *276*, 574–577.
Platt, J. P. (2000), Calibrating the bulk rheology of active obliquely convergent thrust belts and forearc wedges from surface profiles and velocity distributions, *Tectonics*, *19*, 529–548, doi:10.1029/1999TC001121.
Prawirodirdjo, L., Y. Bock, R. McCaffrey, J. Genrich, E. Calais, C. Stevens, S. S. O. Puntodewo, C. Subarya, and J. Rais (1997), Geodetic observations of interseismic strain segmentation at the Sumatra subduction zone, *Geophys. Res. Lett.*, *24*, 2601–2604, doi:10.1029/97GL52691.
Prawirodirdjo, L., R. McCaffrey, C. D. Chadwell, Y. Bock, and C. Subarya (2010), Geodetic observations of an earthquake cycle at the Sumatra subduction zone: Role of interseismic strain segmentation, *J. Geophys. Res.*, *115* B03414, doi:10.1029/2008JB006139.
Philibosian, B., K. Sieh, J.-P. Avouac, D. H. Natawidjaja, H. W. Chiang, C. C. Wu, H. Perfettini, C. C. Shen, M. Daryono, and B. Suwargadi (2014), Rupture and variable coupling behavior of the Mentawai segment of the Sunda megathrust during the supercycle culmination of 1797 to 1833, *J. Geophys. Res. Solid Earth*, *119*, 7258–7287, doi:10.1002/2014JB011200.
Royer, J.-Y., and R. G. Gordon (1997), The motion and boundary between the Capricorn and Australian plates, *Science*, *277*(5330), 1268–1274.
Savage, J. C., and R. O. Burford (1973), Geodetic determination of relative plate motion in central California, *J. Geophys. Res.*, *78*, 832–845, doi:10.1029/JB078i005p00832.
Sieh, K., and D. H. Natawidjaja (2000), Neotectonics of the Sumatran fault, Indonesia, *J. Geophys. Res.*, *105*, 28,295–28,326, doi:10.1029/2000JB900120.
Sieh, K., J. Rais, and Y. Bock (1991), Neotectonic and paleoseismic studies in west and north Sumatra, *Eos Trans. AGU*, *72*, 460.
Sieh, K., J. Zachariasen, Y. Bock, L. Edwards, F. Taylor, and P. Gans (1994), Active tectonics of Sumatra, *Geol. Soc. Am. Abstr. Programs*, *26*, 382.
Singh, S. C., N. D. Hananto, A. P. S. Chauhan, H. Permana, M. Denolle, A. Hendriyana, and D. Natawidjaja (2010), Evidence of active backthrusting at the NE Margin of Mentawai Islands, SW Sumatra, *Geophys. J. Int.*, *180*(2), 703–714.
Storey, M., R. G. Roberts, and M. Saidin (2012), Astronomically calibrated $^{40}Ar/^{39}Ar$ age for the Toba supereruption and global synchronization of late Quaternary records, *Proc. Natl. Acad. Sci. U.S.A.*, *109*(46), 18,684–18,688.
Tikoff, B., and C. Teyssier (1994), Strain modeling of displacement-field partitioning in transpressional orogens, *J. Struct. Geol.*, *16*, 1575–1588.
Wessel, P., W. H. F. Smith, R. Scharroo, J. Luis, and F. Wobbe (2013), Generic Mapping Tools: Improved version released, *Eos Trans. AGU*, *94*(45), 409–410, doi:10.1002/2013EO450001.
Wiseman, K., P. Banerjee, K. Sieh, R. Bürgmann, and D. H. Natawidjaja (2011), Another potential source of destructive earthquakes and tsunami offshore of Sumatra, *Geophys. Res. Lett.*, *38* L10311, doi:10.1029/2011GL047226.
Yeats, R. S., K. Sieh, and C. R. Allen (1997), *The Geology of Earthquakes*, pp. 576, Oxford University Press, Oxford, isbn:9780195078275.